Evidence of gravity wave contribution to vertical shear and mixing in the lower stratosphere: a WISE case study

Madhuri Umbarkar[1], Daniel Kunkel[1], Annette Miltenberger[1], Hans-Christoph Lachnitt[1], Thorsten Kaluza[2], Cornelis Schwenk[1], and Peter Hoor[1]

[1]Institute for Atmospheric Physics, Johannes Gutenberg University Mainz, Germany
[2]Department of Meteorology, University of Reading, Reading, UK

Correspondence: Madhuri Umbarkar (mumbarka@uni-mainz.de)

Abstract. Evidence is presented which illustrates the role of atmospheric gravity wave (GW) induced shear as a mechanism for the occurrence of clear air turbulence and exchange of air masses with different chemical composition in the lower stratosphere. This study investigates the characteristics of GWs and their impact on the distribution of trace species in the lowermost stratosphere during an extratropical cyclone over the North Atlantic using airborne in-situ observations, ERA5 reanalysis data as well as IFS and ICON forecast data. Tracer observations as well as model simulations reveal fine scale structures around the tropopause which are embedded in a region influenced by the inertia gravity waves, warm conveyor belt ascent and mesoscale modifications of the tropopause structure. The GWs propagate through highly sheared flow above the jet stream maximum, perturbing background wind shear and static stability, and thereby creating conditions conducive to turbulent mixing in the lowermost stratosphere. The observed significant correlation between GW-induced momentum flux and enhanced shear perturbations confirms the role of GWs in driving potential turbulence and facilitating trace gas exchange in the lower stratosphere. Further analysis of turbulence diagnostics suggests that GWs produce shear which leads to the occurrence of clear air turbulence.

1 Introduction

Atmospheric gravity waves (GW), ubiquitous buoyancy-driven oscillations, play a crucial role in a wide variety of atmospheric processes. These gravity waves can initiate and organize convection (Zhang et al., 2001), as well as generate and modulate atmospheric turbulence (Shapiro, 1980). Also, large amount of momentum and energy can be propagated and transferred by GWs, which results in an impact on the general circulation, especially for exchange of air masses between troposphere and stratosphere (Holton et al., 1995).

Generally speaking, GWs can be generated and activated by topographic forcing, convection, shear instability, as well as geostrophic adjustment related to jets, fronts, and sources of strong diabatic heating (Hooke, 1986; Fritts and Alexander, 2003; Kim et al., 2003; Plougonven et al., 2008). Orographic GWs are generated through the interaction between atmospheric flow and surface topographic features, producing mainly vertically propagating waves that influence the energy and momentum balance in the UTLS (Durran, 1995; Lachnitt et al., 2023). These GWs propagate further upwards through the stratosphere

where they dissipate and influence the atmospheric circulation, particularly the Brewer-Dobson circulation (BDC) (Achatz

25 et al., 2024, and reference therein). Convective sources generate GWs through latent heat release and rapid vertical motions as in thunderstorms, often observed in both tropical and extratropical regions (Fritts and Alexander, 2003; Alexander et al., 2010). Moreover, Lane et al. (2001) and Lane and Sharman (2006) emphasized that convective clouds generate GWs when the convective updraft rapidly decelerates. The distribution of different GW sources largely controls the global distribution of GWs and GWs impact on atmospheric stability and transport processes.

30 In the extratropics, baroclinic waves represent an important, albeit less well understood source of GWs. Surface fronts and upper level jet streams associated with baroclinic wave development generate GWs, primarily through spontaneous imbalance, i.e., deviations from balanced flow trigger wave emission (Plougonven and Zhang, 2014; Zhang et al., 2015b). Regions of baroclinic instability, particularly along jet streaks and frontal zones, are hotspots for non-orographic GW activity. In such regions, interactions between divergent flow (or GWs) and the background flow (Trier et al., 2020) lead to shear generation

35 and turbulence (e.g., O'sullivan and Dunkerton, 1995; Plougonven and Snyder, 2005; Zülicke and Peters, 2006; Kaluza et al., 2021). Baroclinic life cycles, as persistent large–scale midlatitude wave patterns, play a pivotal role in modulating large–scale circulations. They influence the BDC by vertically transporting momentum and energy, influencing jet dynamics, and affecting the potential vorticity distribution in the UTLS (Alexander et al., 2010; Achatz et al., 2024, and references therein). Their influence also extends to the tropopause structure and stratosphere–troposphere exchange (STE) processes, that relate the

40 small-scale dynamics with planetary scale overturning circulation (Plougonven et al., 2008; Kunkel et al., 2014; Dörnbrack, 2024; Jovanovic, 2025). Despite their ubiquity, the mechanisms governing GW generation within baroclinic system remain poorly understood, necessitating further investigation to quantify their role in shaping the UTLS and beyond.

Orographic GWs, despite exhibiting significant seasonality and a high degree of transience, serve as hotspots for turbulence at the tropopause (Fritts and Alexander, 2003; Alexander and Grimsdell, 2013; Rapp et al., 2021). Lachnitt et al. (2023) have

45 shown that GW induced turbulence can have a persistent effect on the distribution of species and hence potential forcing impact on radiatively active tracer species by changing their isentropic gradients (Dörnbrack et al., 2025). Consequently, the mixing induced by GWs contributes to the overall mixing-induced uncertainty of radiative forcing (Riese et al., 2012).

GWs likewise play a key role in shaping the thermodynamic structure of the UTLS by either enhancing vertical wind shear or reducing static stability (Kunkel et al., 2016; Kaluza et al., 2021; Dörnbrack, 2024). These interactions contribute to the

50 formation of an enhanced shear layer in the extratropics so called "tropopause shear layer" (TSL, Kaluza et al., 2021). The TSL is typically identified as the region near the extratropical tropopause where shear exceeds a critical threshold S_t^2, typically the 95th percentile of climatological dataset. Such pronounced shear is often linked to tropopause disturbances and has been observed on the order of 10^{-2}–$10^{-3}\,\mathrm{s^{-1}}$ (Lane et al., 2004; Kaluza et al., 2021), occurring particularly in dynamically active regions such as jet streaks and frontal zones (Koch et al., 2005; Wang and Zhang, 2007), where clear air turbulence (CAT)

55 is also common. GWs also influence the tropopause inversion layer (TIL) through wave breaking and momentum deposition, reinforcing its stratification and affecting exchange of air masses between stratosphere and troposphere (or within the lower stratosphere) (Kunkel et al., 2014; Zhang et al., 2015b; Kunkel et al., 2019). However, a comprehensive analysis of these

processes often remain sensitive to model resolution or limited observations and as such pose a challenge for both modeling and observational studies (Plougonven and Zhang, 2014; Stephan et al., 2019a; Geller et al., 2013; Jewtoukoff et al., 2015).

60 GWs influence tracer transport and mixing in the UTLS by generating turbulence, either through enhanced vertical shear that triggers instabilities like Kelvin–Helmholtz instability (KHI) or through wave breaking at critical levels where GW phase speed aligns with the background wind (e.g., Shapiro, 1978; Whiteway et al., 2004; Lane and Sharman, 2006). These processes are particularly active in the extratropical transition layer (ExTL), a tracer-defined mixing zone around the tropopause that is prone to cross-isentropic exchange between stratospheric and tropospheric air masses (Hoor et al., 2004; Pan et al., 2006;
65 Hegglin et al., 2009). The ExTL overlaps with the lower part of the lowermost stratosphere (LMS). While the ExTL is situated around the extratropical tropopause, usually defined as an isosurface of potential vorticity, the LMS is the region between the extratropical and the tropical tropopause, bounded above by the 380 K isentrope (Weyland et al., 2025; Appenzeller et al., 1996; Holton et al., 1995; Olsen et al., 2013; Wang and Fu, 2021). The ExTL and LMS are the regions with strong vertical gradients of chemical species which result from the different dynamical and partly chemical processes in the stratosphere and
70 troposphere. In the extratropics, quasi-isentropic transport plays a crucial role for the constituent exchange in the ExTL as has been shown by trajectory-based analyses (Berthet et al., 2007; Hoor et al., 2010) and by airborne observations (e.g., Hoor et al., 2004; Pan et al., 2004; Kunkel et al., 2019). Additionally, small–scale mixing events affects the tracer gradients locally, often in relation to shear instabilities or convection (e.g., Whiteway et al., 2003; Lane et al., 2004; Zhang et al., 2015b; Lachnitt et al., 2023; Dörnbrack et al., 2025).

75 Observations from aircraft and radiosondes confirm that turbulence in the ExTL enhances vertical mixing of key tracers like ozone and water vapor, affecting UTLS composition and radiative balance (Birner et al., 2002; Birner, 2006; Hoor et al., 2004; Zhang et al., 2015a; Heller et al., 2017). GWs modulate potential vorticity (PV) gradients near the tropopause and drive mixing via shear-induced instabilities (Spreitzer et al., 2019). Beyond its relevance to aviation, CAT also contributes to cross-tropopause transport of chemical constituents and plays a significant role in modulating large–scale atmospheric circu-
80 lation. Simulations of midlatitude cyclones highlight the role of jet dynamics and GWs in CAT generation (Lane et al., 2004; Trier et al., 2020). However, forecasting CAT remains challenging due to its intermittent nature and small–scale motion (with turbulent eddies typically spanning horizontal scales of ∼10 to 1000 m), compared to the resolution of current numerical weather prediction models (Sharman et al., 2006, 2014; Sharman and Pearson, 2017). These motivates further investigation into GW-driven mixing, its contribution to the CAT and its influence on ExTL structure.

85 Our primary goal is to investigate the contribution of GWs to tropopause following shear enhancement within the extratropical UTLS (ExUTLS) over the North Atlantic during a life cycle of an extratropical cyclone, as revealed by the idealized baroclinic life cycle experiments in Umbarkar and Kunkel (2025). First, we present an evidence of observed recent air mass mixing during a flight of the WISE (Wave-driven ISentropic Exchange) mission. Second, we examine whether this mixing event is linked to enhanced shear and GW activity (Sect. 3). Third, we examine the representation of shear and the associated GW-
90 induced turbulent mixing in ERA5, IFS, and ICON over the North Atlantic during this event in the UTLS (Sect. 4). The last point is related to the question whether ERA5 is good enough resolved to study GWs, shear and mixing in the UTLS in case

studies, and thus potentially also in a climatological context. Furthermore, we also investigate whether instabilities triggered by GW-induced shear can lead to the development of CAT.

2 Data and methods

2.1 In situ measurements

95 In autumn 2017, the WISE (Wave-driven ISentropic Exchange) mission was conducted using the German HALO (High Altitude and Long Range) research aircraft, operating from Oberpfaffenhofen, Germany, and Shannon, Ireland. In this study we focus on research flight 05 (RF05) on 23rd September 2017 between 08:09 and 17:04 UTC. The goal of this flight was to investigate the dynamical and chemical structure of the atmosphere in the vicinity of the tropopause over the North Atlantic

100 between Ireland and a region north of Iceland in a far north reaching subtropical intrusion.

During the WISE campaign, HALO was outfitted with a specialized suite of instruments for in situ and remote sensing. Our analysis is mainly based on in-situ measurement of CO and N_2O from UMAQS (University of Mainz Airborne Quantum Cascade Laser Spectrometer, Müller et al., 2015). For the WISE campaign, the total drift-corrected uncertainty was determined to be 0.94 ppbv for CO and 0.18 ppbv for N_2O (Kunkel et al., 2019). Additionally, we use meteorological parameters measured

105 with BAHAMAS (Basic HALO Measurement and Sensor System, Krautstrunk and Giez, 2012; Kunkel et al., 2019).

2.2 ERA5 reanalysis data

As a reference for the zonal and meridional wind components and as the basis for additional meteorological context, ERA5 the most recent reanalysis produced by the European Center for Medium-Range Weather Forecasts 5th generation (ECMWF, Hersbach et al., 2020) is used. It is based on 4DVar data assimilation and model forecast using cycle Cy41r2 of the ECMWF

110 Integrated Forecasting System model. The model data is available on 137 model levels from the surface to 0.01 hPa with a vertical grid spacing of roughly 300 m in the UTLS. The model level data has further been interpolated on height, pressure and isentropic levels for our analysis. In this study, two ERA5 based products are used: (i) data extracted along the flight path used in Sect. 3 (Lachnitt, 2025) and (ii) four-dimensional meteorological fields with hourly time resolution and on horizontal grid with 0.25° in latitude and longitude, used in Sect. 4.

115 ### 2.3 IFS forecast data

Next, we use ECMWF IFS operational forecast data as a high resolution companion of the ERA5 reanalysis. The data is based on IFS cycle 43r3 and analyzed on a regular 0.1° latitude-longitude grid with hourly temporal resolution. Also this data is of interest because the IFS version used to produce this forecast is very close to the version used for ERA5 production. The operational IFS employs a Tco1279 spectral truncation and an associated O1280 octahedral grid which results in an $\Delta x \approx 9$

120 km grid spacing in the horizontal and incorporates 137 vertical levels, derived from the operational analysis data. This data has almost the same dynamical core and physical package as ERA5 which allows to study the effect of higher horizontal resolution

on the representation of the shear and GWs. We use the operational forecast from 23 September 2017 00 UTC, with hourly resolution for the first 24 hours.

2.4   ICON forecast

125   In addition, we use ICON simulation data of this case from Schwenk and Miltenberger (2024). This allows us to study the representation of the same situation in a model with a different dynamical core and physics package as well as in three different resolutions from roughly the resolution in IFS data to almost convection permitting resolution. As such we can directly test how robust our findings are across different model representations. In particular, the atmospheric evolution for this case was simulated using the high resolution ICOsahedral Nonhydrostatic (ICON) modeling framework (version 2.6.2; Zängl et al.,
130   2014) over the North Atlantic Ocean. The simulation was initialized with the operational ICON global analysis at 00:00 UTC on 20 September 2017, shortly before the cyclone developed, and ran for 96 hours, ending at 00:00 UTC on 24 September 2017, when the warm conveyor belt dissipated over northern Europe. The global ICON model simulation on R03B07 grid (effective resolution of ∼13 km) with a 120 s time step, contained to nested regions using R03B08 (∼6.5 km) and R03B09 (∼3.3 km) grids with 60 s and 30 s time steps, respectively. Figure 1c illustrates the ICON nested setup and atmospheric situation over the
135   study region at 11:00 UTC on 23 September 2017.

2.5   Deriving resolved gravity wave momentum fluxes and turbulence diagnostics

The GW activity in the model outputs is analyzed via two diagnostic variables: the horizontal divergence $\nabla_h u_h$ and the absolute momentum flux due to GWs. The model horizontal divergence field is used to identify GW prone regions. Furthermore, in order to understand momentum transport due to small scales and occurrence of GWs, we restrict ourself here to the presentation of
140   gravity wave vertical fluxes of horizontal momentum in terms of distribution of probability density functions (PDFs). The vertical transport due to small–scale processes in the ExUTLS is investigated via absolute momentum flux (AMF). Here the fluctuations of short-scales from the large–scale background flow are referred to the small–scale perturbations induced by gravity waves (hereafter GW perturbations). Note that, the momentum flux of the sub-synoptic scales, which we refer to as a first proxy for the momentum flux due to small–scale GWs.
145   The GW perturbations from synoptic-scale structures are quantified using a hybrid method that combines a dynamical with a statistical approach to separate large and small–scale components of the flow (similar to Wei et al., 2022). We first divide the flow in its divergent and rotational components through the application of a Helmholtz decomposition, i.e., the dynamical approach. For the so called statistical component, we then apply a filter in spectral space using a one-dimensional zonal FFT over the full domain displayed in Fig. 1. With this additional spectral filter we remove the contributions from wavenumber 0
150   to 20, i.e. $u' = u_{\mathrm{div}} - (u_{\mathrm{div}})_{k \leq k_s}$, where $k_s = 20$, is the wavenumber cutoff that splits respective quantities into a large–scale and small–scale components. The latter is the perturbation from synoptic-scale structures and is from now on denoted with primes. Note here that sensitivity tests with k_s values of ± 4 showed no significant variation in the resulting primed quantities. The

deviation of small–scale from large–scale flow are shown in Fig. A1. The AMF is then computed from perturbation fields as:

$$\text{AMF} = \rho \sqrt{(\overline{u'w'})^2 + (\overline{v'w'})^2} \tag{1}$$

155   where ρ is the mean density, and u', v', and w' are the zonal, meridional, and vertical velocity perturbations, respectively. The overline showcasing the perturbation products (i.e. $\overline{u'w'}$ and $\overline{v'w'}$) is computed with a low-pass filtering of the quadratic quantities which uses the same Gaussian spectral filter as in Kruse and Smith (2015). We emphasize that our hybrid approach for separating synoptic and sub-synoptic scale flow is well justified in the UTLS (Zhang et al., 2025) and follows the commonly used GW scale separation methods as in Lehmann et al. (2012); Wei et al. (2016); Stephan et al. (2019a); Strube et al. (2020);

160   Gupta et al. (2021); Wei et al. (2022); Umbarkar and Kunkel (2025), despite different cutoff wavenumber being used in different studies.

Another key diagnostics is the vertical shear:

$$S^2 = \left(\frac{\partial u}{\partial z}\right)^2 + \left(\frac{\partial v}{\partial z}\right)^2. \tag{2}$$

This quantity can also be derived from the wind perturbations and will be denoted as $S^{2'}$ in the following. Turbulence diag-

165   nostics and their constituents are computed as outlined in Sharman et al. (2006). The regions with potential for turbulence occurrence are identified via two meteorological parameters: the gradient Richardson number Ri and the Ellord turbulence indices, TI1 and TI2. The use of multiple diagnostics is motivated by the need to capture both dynamical and kinematic aspects of turbulence generation in the ExUTLS, especially to asses the regions affected by GW-induced shear and mixing. Instabilities being a key prerequisite for mixing of air masses in the atmosphere, such as KHI, can be identified using Ri,

170    $$Ri = \frac{N^2}{S^2} = \frac{\left(\frac{g}{\theta}\frac{\partial \theta}{\partial z}\right)}{\left(\frac{\partial u}{\partial z}\right)^2 + \left(\frac{\partial v}{\partial z}\right)^2} \tag{3}$$

i.e., the ratio of static stability (N^2) to vertical wind shear (S^2). Regions with $Ri \leq 0.25$ are theoretically considered to be dynamically unstable and prone to KHI. In contrast, when using a value from resolved model quantities, a slightly weaker criterion is often applied and regions with Ri on the order of 1 are considered to be dynamically unstable. Note that the total vertical wind shear is used to compute Ri, in order to initially evaluate regions susceptible to turbulence within the baroclinic

175   flow.

While Ri captures dynamic instability, it may not fully represent turbulence under complex flow conditions. To account this limitation, we also employ the Ellord-Knapp turbulence indices, TI1 and TI2, which are empirical diagnostics specifically developed to identify CAT. The Ellord-Knapp Turbulent Index (TI1), has been shown to be capable of detecting 70%–84% of CAT occurrences (e.g., Ellrod and Knapp, 1992; Sharman and Pearson, 2017; Kim et al., 2018; Gultepe et al., 2019; Thompson

180   and Schultz, 2021), making it a valuable complement to dynamically based measures. We resort this to the small scales, ensuring that potential turbulence in the subsequent analysis reflects subgrid or small–scale contributions. TI1 (Ellrod and Knapp, 1992), a well established turbulence indicator combines vertical wind shear perturbations and the total flow deformation

(DEF), whereas TI2 adds the contribution from convergence (CVG). The TI1 is calculated using;

$$\text{TI1} = \text{S} \times \text{DEF} \tag{4}$$

185 whereas, TI2 is derived using;

$$\text{TI2} = \text{S} \times (\text{DEF} + \text{CVG}) \tag{5}$$

where S is the magnitude of vertical wind shear perturbations ($S^{2'}$) as defined in Eq. 2. DEF is the total flow deformation:

$$\text{DEF} = \left(\left(\frac{\partial u}{\partial x} - \frac{\partial v}{\partial y} \right)^2 + \left(\frac{\partial v}{\partial x} + \frac{\partial u}{\partial y} \right)^2 \right)^{1/2} \tag{6}$$

and convergence is calculated according to,

190 $$\text{CVG} = - \left(\frac{\partial u}{\partial x} + \frac{\partial v}{\partial y} \right) \tag{7}$$

Here, both CVG and DEF are consistently derived from the perturbation wind components (u', v'), and thus TI1 and TI2 are likewise based only on the corresponding prime quantities. The inclusion of CVG in TI2 offers an advantage over TI1 by capturing the small–scale flow features such as those associated with GWs or upper level frontal structures. These region often exhibit enhanced shear and convergence making TI2 more sensitive to turbulence driven by mixing processes.

195 Note that, for the analysis of occurrence frequencies in Sect. 4, all datasets were regridded to ERA5 horizontal grid (0.25° resolution) for the purpose of intercomparison, such that remaining differences primarily reflect the model frameworks and dynamics as well as resolution effect.

3 Analysis of GW induced mixing in a baroclinic wave over Iceland

3.1 Meteorological situation

200 The major goal of the flight was to determine whether trace species show specific signatures of irreversible mixing in regions of enhanced static stability in the lower stratosphere. We took advantage of this flight data and further ask whether this irreversible mixing event occurs in regions of GW-induced shear enhancement. The flight was planned in the ridge of a synoptic-scale baroclinic wave which evolved during the previous days over the North Atlantic at the edge of large–scale trough.

We start with a description of the atmospheric situation over the North Atlantic during the time which we focus on in the
205 subsequent analysis. The isentropic distribution of potential vorticity (PV) on 340 K in Fig. 1a-c illustrates the meteorological situation during research flight number 5 of the WISE campaign (in following denoted as WISE RF05) for ERA5, IFS and ICON, respectively. The synoptic situation in the UTLS at 11:00 UTC over the North Atlantic Ocean on September 23, 2017 (Fig. 1a) is dominated by the strong meridional excursion of the sub-tropical air masses far north in a region from the Iberian peninsula over Great Britain up to Iceland. The tropospheric streamer is embedded between two equatorward reaching
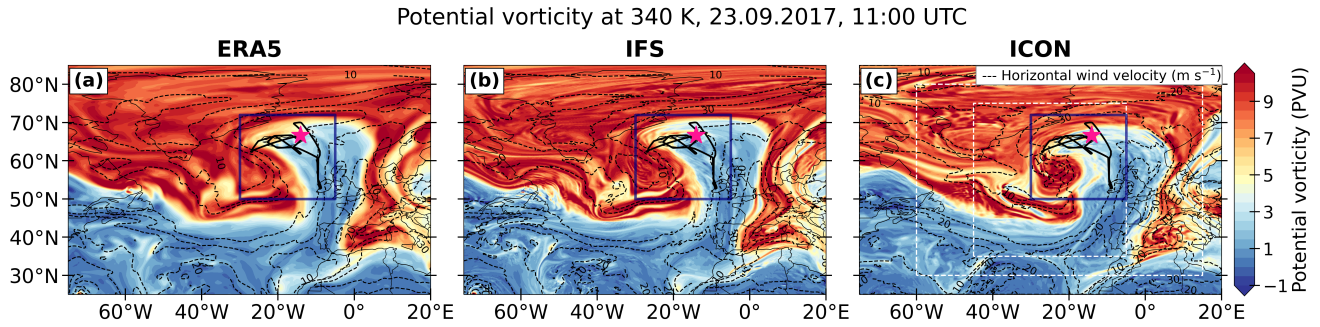
Figure 1. Potential vorticity distribution (in PVU) at the 340 K isentropic surface on 23.09.2017 at 11 UTC for (a) ERA5, (b) IFS forecast, (c) ICON model data. The dashed lines show the horizontal wind (in m s^{-1}) on 340 K. The thick black line shows the flight path of RF05 and the star marks the aircraft position at 11 UTC.

stratospheric streamers, the one to the west being more coherent in its structure, while the one to the east shows more internal structure in terms of its isentropic PV.

The flight went from Shannon, Ireland towards Iceland where a hexagon was flown as well as a dive was performed before returning to Shannon. The flight track is shown by the black line in Fig. 1. The PV distribution shows that the flight took place to a large degree in the region where subtropical air masses, around 11-13 km, moved polewards while some parts of the flight track also reached across the PV gradient into the lower stratosphere. The region of the strong PV gradient corresponding to the location of the jet stream acts as a barrier between tropospheric and stratospheric air masses. On the large–scale, all three model data sets show similar patterns in terms of the overall PV distribution. Moreover, smaller-scale ripple-like structures in the PV field around 20° W and 65° N (Fig. 1c) could signify wave activity, which are often generated near jet streams or strong dynamical forcing regions, as reported e.g., for RF07 from WISE (Kunkel et al., 2019). Such small–scale wave like structures in the PV field in the transition region between tropospheric and stratospheric air masses could already hint towards the presence of GWs associated with mixing of air masses. In the next sections we look deeper into the observational data from WISE RF05.

3.2 Identification of flight segments affected by turbulence

We first examine the time series of measured and ERA5 quantities interpolated to the aircraft position during WISE RF05. The goal is to identify regions and periods of potential turbulence and small–scale mixing above the tropopause.

Figure 2 shows a comparison of in situ measured atmospheric state parameters including chemical tracers and potential temperature (a) and instability parameters (b) from the ERA5 reanalysis data that was interpolated in time and space onto the flight path. The pressure measured during WISE RF05 shows that the flight path was designed to ascend with time (Fig 2a). An exception is the dive between 13:00 UTC and 14:00 UTC. This ascend is also mirrored in the decrease of N$_2$O with time and the associated increase of potential temperature and ERA5 potential vorticity. In contrast, ERA5 vertical shear S^2 and Richardson number Ri show a more diverse temporal evolution. In particular, shear maximizes (up to $\geq 4 \times 10^{-4} s^{-2}$) and Ri
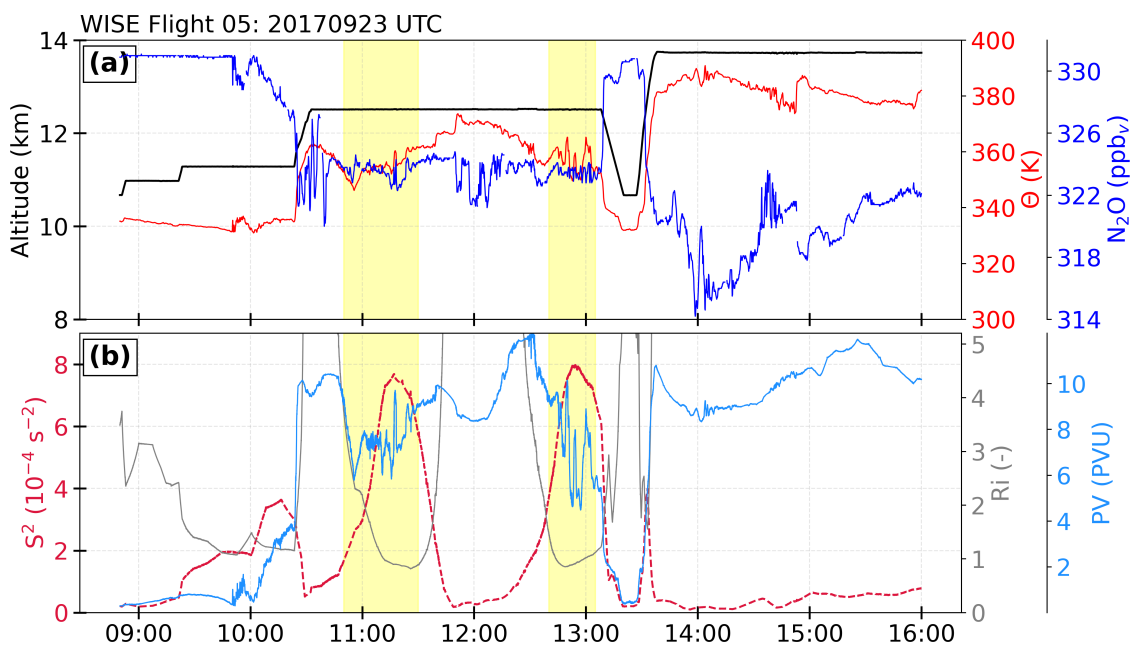
Figure 2. Time series of (a) observed flight altitude (in km, black), potential temperature (in K, red), and nitrous oxide (in ppbv, blue) as well as (b) ERA5 derived quantities along the flight path such as vertical shear (in 10^{-4} s^{-2}, red), Richardson number (dimensionless, grey), and potential vorticity (in PVU, cyan). The light yellow bars and the white bar in between indicate the flight section of the consecutive detailed analysis of mixed air masses.

shows minima around 11:15 UTC and 13 UTC with values below 1 (Fig. 2b). These two time periods are surrounded by times with rather low shear values and high Ri along the flight track. In a next step, we examine these time periods and events in more detail using tracer-tracer correlations.

235 ### 3.3 Trace gas observations, the role of gravity waves and small–scale mixing

For the identification of small–scale mixing, we examine tracer-tracer correlation based on measurement data. We use trace gases suggesting a tropospheric origin on one side, i.e., CO, and trace species indicative of stratospheric air masses, i.e., N_2O on the other side.

We focus on the time period between 10:45 UTC and 13:05 UTC which is the time period bounded by the two yellow marked

240 regions in Fig. 2. During this time HALO was flying in the LMS with potential temperature values between 330 K and below 380 K. The measurements took place just above the region of the strongest vertical gradients of CO and N_2O where the vertical gradient becomes small again (Fig. 3a, b). Since one would generally expect vertical gradients of N_2O over this potential temperature range, the almost vertical profile is a first indication of a process which mixes or having mixed (i.e. homogenized) air masses prior to the measurements in this altitude range. Additionally, the mixing ratios of CO and N_2O are well below
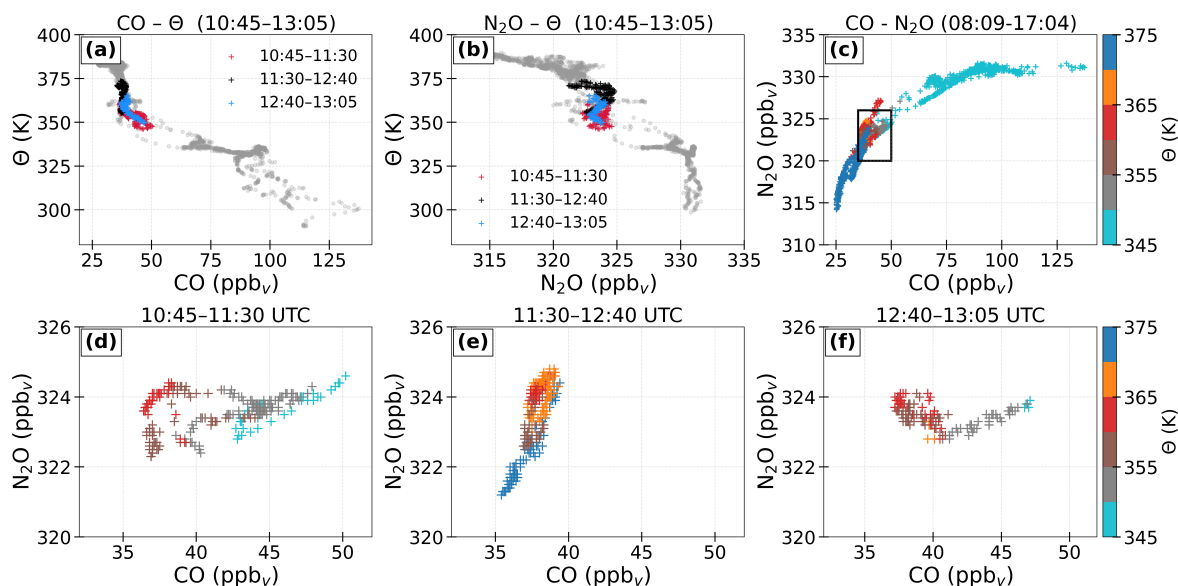
Figure 3. Vertical profiles of (a) CO (in ppbv) and (b) N_2O (in ppbv) with grey circles showing data of the entire flight and color-coded markers indicating the time from 10:45-13:05 UTC. (c-f) Tracer-tracer correlation of the mixing ratios of N_2O and CO for (c) the entire flight and for time periods between (d) 10:45-11:30 UTC, (e) 11:30-12:40 UTC and (f) 12:40-13:05 UTC, color-coded with potential temperature.

245   their tropospheric background values, which is also evident in the CO-N_2O correlation (Fig. 3c). The part of the correlation highlighting the time period of interest (marked region) is rather located in the stratospheric branch and partly within the transition region between stratosphere and troposphere. These regions are characterized by low CO and N_2O mixing ratios, with N_2O values below the well-defined tropospheric background of 331 ppbv during WISE RF05 (see also Kunkel et al., 2019). More so, we expect to find a monotonic correlation between CO, N_2O and potential temperature Θ. The mixing ratios of

250   CO and N_2O should decrease as an air mass becomes more stratospheric, whereas potential temperature should simultaneously increase. On first glance this relation is evident in the correlation and profiles shown in Fig. 2. However, deeper inspection of the correlation in the time period of interest, as discussed below, highlights some deviations from this relation. In turn, such deviations can be linked to recent mixing (e.g., Kunkel et al., 2019; Lachnitt et al., 2023).

For further inspection we split the correlation into three time periods: i) 10:45 -11:30 UTC (Fig. 3d), ii) 11:30 - 12:40 UTC

255   (Fig. 3e) and iii) 12:40 - 13:05 UTC (Fig. 3f). This results in some interesting findings. The first shorter time period exhibits two branches which are interconnected with a mixing line (at around $N_2O \sim 324$ ppbv, $\Theta \sim 359$ K). In the second time period, one branch is evident which shows rather Θ values spread over the entire branch, meaning that no fixed relation between Θ and the tracer is evident although CO and N_2O show a compact positive correlation. In the third time period almost all data points reside in a very small domain in the correlation space with potential temperature values varying strongly over this domain.

260   All of these findings are potential indications that these air masses have been subject to a process which breaks the relation between CO, N_2O, and Θ; one potential process which can lead these correlations is mixing. It is interesting to note that the

first and third time periods show indications of recent mixing, where the ERA5 analysis shows indications of recent turbulence
occurrences (Fig. 2b). Meanwhile, the second time period appears closer to the equilibrated background CO-N_2O relation.
This could indicate that the first and third event have been subject to more local recent mixing, while the air mass in between
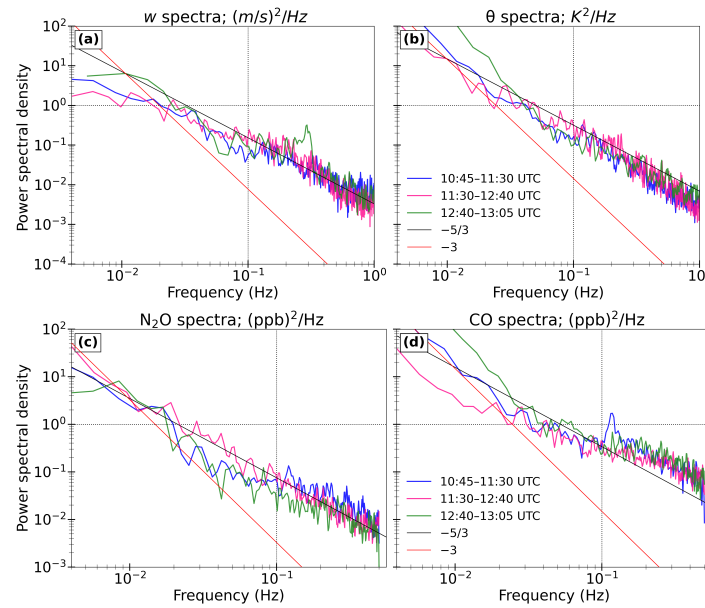265 has been mixed some time ago.

Figure 4. Power spectral densities of (a) measured vertical velocity (in (m/s)^2/Hz) and (b) observed potential temperature (in K^2/Hz) from
BAHAMAS, and of (c) N_2O (in ppbv)^2/Hz) and (d) CO (in ppbv)^2/Hz) from UMAQS during WISE RF05 for the time periods 10:45-11:30
UTC (blue lines), 11:30-12:40 UTC (red lines) and 12:40-13:15 UTC (green lines). The orange line indicates the slope of -3 (geostrophic
turbulence), the thin black line a slope of -5/3 (mesoscale turbulence).

An analysis of power spectral densities of w, Θ (Fig. 4a, b) and N_2O, CO (Fig. 4c, d) also reveals the presence of small–scale
turbulent processes. All spectra rather have a slope of -5/3 which is often seen as an indication for turbulence occurrence on the
mesoscale and below (e.g., Zhang et al., 2015a; Dörnbrack et al., 2022; Lachnitt et al., 2023). Particularly, the small transition
between slopes observed in N_2O spectra around 10^{-2} Hz (green and blue lines), where the slopes of w indicates turbulent
270 energy source, and here, the N_2O hints the turbulent behavior of small scales, e.g., those related to GWs, might be substantial
to explain the dynamics in the lower stratosphere.
The question on how much GW contribute to the mixing of these air masses is difficult to answer based on the observations
along the flight path. Before we broaden our scope in the analysis to the synoptic scale, we further attempt to provide further
observational evidence for GWs signatures during the measurements. The close spacings of the measurements shown in Fig.
275 2 allows the detailed mesoscale structures of the jet/front to be elucidated, including low Ri, and possible coherent phase
structures of GWs. Nonetheless, the (time interval) resolution of in situ measurements is too large to properly sample waves
with horizontal wavelengths of $\sim$100 km in hourly model output data. However, the aircraft flew high enough to identify

coherent phase lines and/or mixing lines in the lower stratosphere such as those observed in Fig. 3.

Hodographs, which depict the variation of horizontal wind disturbance vectors in velocity space, typically show an elliptical
280   shape in presence of inertia GWs (Hirota and Niki, 1986). Given the high resolution of the measurements, the hodograph
techniques can be utilized to identify the presence of inertia GWs and its characteristics (e.g. Guest et al., 2000; Lane et al.,
2004; Yoshida et al., 2024). Although, hodographs can be drawn from vertical profiles at a time, given that limited altitude level
data, in our analysis a single hodograph is drawn using profiles at multiple times at one flight altitude (e.g., as in Gomes et al.,
2025). Figure 5 shows example hodographs for the period of interest where the indication of mixing have been observed. Note
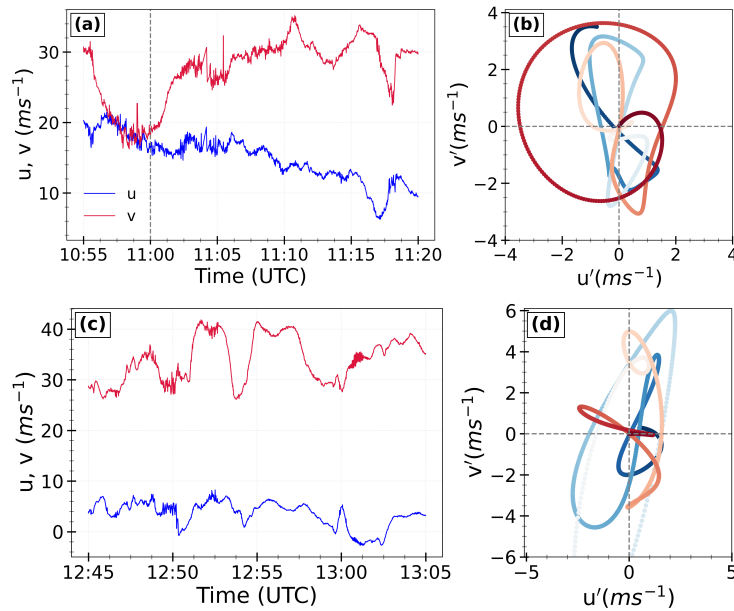
Figure 5. Time series (a, c) of zonal (u, in m s^{-1}; blue) and meridional (v, in m s^{-1}; red) wind component measured during WISE RF05
zoom in for time 10:55–11:20 UTC and 12:45–13:05 UTC. Perturbation hodographs for the corresponding flight period are shown in panels
(c) and (d), with trajectories starting in red and ending in blue.

285   that, to isolate wind perturbations associated with GWs from the background wind, horizontal wind components (u, v) along
the flight track were bandpass filtered using a 4th order Butterworth filter. The filter was applied to remove both large–scale
trends and high-frequency noise, retaining signals within a 2–10 minute period range. The resulting perturbations (u', v') were
then used to construct hodographs and to assess wave properties from the in situ measurements. These perturbation time series
are shown in Fig. B1. Due to distinct sampling frequencies and noise characteristics, separate filtering methods were applied
290   to flight and model datasets to optimally isolate GW related perturbations.

Linear theory of GWs in a uniform background flow predicts that one vertical wavelength of an inertia GW traces an elliptical
perturbation hodograph (as described in Guest et al., 2000; Plougonven et al., 2003; Yoshida et al., 2024), which rotates
anticyclonically (cyclonically) for an upward (downward) propagating wave. This technique has some limitations in terms of

295   conditions with strong background wind shear and hence is only suitable for a part of the wave spectrum with low-frequency, long-wave limit (for more details see Plougonven et al., 2003). This technique is applied to time series of u', v' at ∼12.5 km flight altitude. The respective time series of u, v is shown in Fig. 5a and 5c (see also Fig. B1). Of these two selective periods, representing multiple ellipses, only few segments show clear evidence of anticyclonically rotating hodographs, i.e., those line segments colored in red in Fig. 5b, d. A well-defined elliptical pattern is evident in Fig. 5b, indicating the presence of upward-propagating GWs. In contrast, although wave-like oscillations are more prominently observed during 12:45-13:05 UTC (Fig.

300   B1), such a coherent elliptical structure is less apparent in Fig. 5d. Based on this, we focus our subsequent GW-shear analysis around 11:00 UTC, where the wave activity appears most pronounced. Moreover, as we will show later in the analysis of the model data, these profiles give an estimates of horizontal and vertical wavelength that are similar to those determined from the models. Also, the limited altitude region here means that only one or two vertical wavelengths are sampled, which adds some uncertainty to the analysis.

305   Nonetheless, this further motivates an in-depth, model supported analysis to understand whether GWs and GW-induced shear are responsible for observed turbulence and mixing. In the next section, we further investigate this in detail from the model perspectives.

4   Gravity waves and turbulence occurrence

In this section we continue our analysis using model data from ERA5 reanalysis, IFS forecast and ICON model simulations to
310   examine whether these datasets provide indications of GW-induced turbulence. Our primary goal is to first analyze similarities and differences in the occurrence of GWs among these datasets for the time of our case study over the North Atlantic. In the subsequent sections, we will then explore the relation between these GWs, vertical wind shear and turbulence. Note that we limit our analysis to the region covered by all models, which includes the entire flight and is defined as 50° N-72° N and 5° W-30° W. The analysis domain is marked in blue in Fig. 1.

315 ### 4.1   Analysis of gravity waves

We start with the horizontal divergence field to identify location and characteristics of potential GW signatures in the lowermost stratosphere. Figure 6a-c shows the horizontal divergence at 12.5 km (∼ 200 hPa) for (a) ERA5, (b) IFS, and (c) ICON datasets. In ERA5, the alternating signatures of divergence-convergence, representing GWs features, are evident near the jet streak exit region, with enhanced activity between 60° N-72° N, particularly over and to the east of Iceland along the flight track (Fig.
320   6a). The IFS forecast shows similar large–scale patterns but resolves additional small–scale GW features over the northeastern Icelandic highlands (see Fig. 6b), a region coinciding with observed signatures of mixing (Fig. 3). On the other hand, ICON captures GW activity over Iceland with moderate amplitudes in the northwestern sector (Fig. 6c), but large amplitude small–scale features similar to IFS. These differences suggest that the nominal resolution largely controls the magnitude of the GW fluctuations in reanalyses and forecasts. The corresponding vertical cross sections at 14.05° W representing the approximate
325   flight location at 11:00 UTC (marked by the dashed line), are shown in Fig. 6d-f.
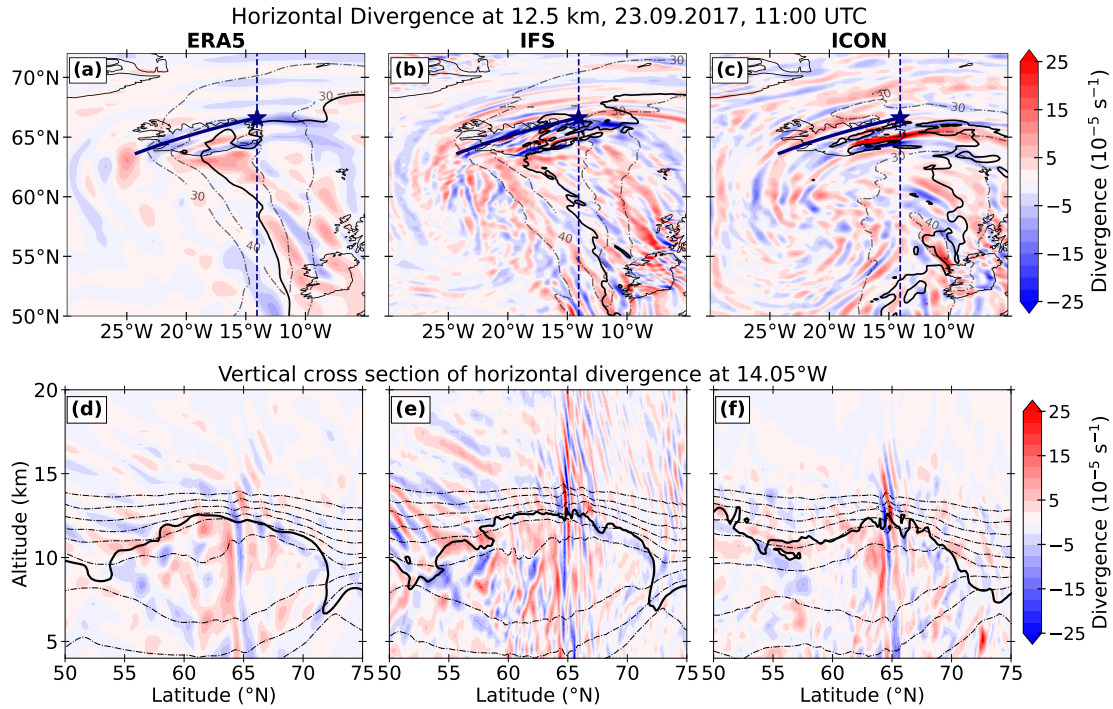
Figure 6. Distribution of horizontal divergence at 12.5 km altitude for a) ERA5, b) IFS and c) ICON datasets. The dashed lines in upper panel represent corresponding horizontal wind speed for values greater than 30 m s^{-1}. The RF05 flight path from 10:55 to 11:45 UTC is indicated in blue, HALO location at 11 UTC shown by blue star. The corresponding vertical cross sections of divergence at 14.05° W is shown in lower panel (d-f). The solid black line represent the 3.5 PVU as a dynamical tropopause whereas dashed lines in lower panel represent the potential temperature starting from 280 K (bottom) to 380 K (top) with 10 K increments.

We define the extratropical tropopause based on the dynamical tropopause definition with a value of 3.5 PVU (1 PVU=1×10^{-6} K m^2 kg^{-1} s^{-1}). In Fig. 6d-f, the thick solid line marks the dynamical tropopause, however, the GW activity influence this. In ERA5, undulations in the PV field are the signatures of upward propagating GWs, with wave amplitudes extending through the lower stratosphere. The observed packet propagates only a short horizontal distance, while spanning vertically up to ∼17.5

330   km in altitude, suggesting a low ground-based phase speed and a narrower vertical wavelength. IFS resolves finer horizontal structures and larger amplitudes with a notably shorter vertical wavelength of ∼2-3 km (Fig. 6e), while ICON shows a similar vertical structure, with a slightly shorter vertical wavelength of ∼3 km (Fig. 6f). However, much more fine-scale signals in IFS and rather lower in the other two, indicates that the GWs characteristics, especially horizontal details are strongly influenced by the spatial resolution. Of interest is the fact that ERA5 despite its much lower horizontal resolution, is able to capture the

335   appearance of GWs in the LMS. Across all three datasets, the GW packet exhibits a similar overall structure. Moreover, the large amplitude wave signatures pointing towards the strong upward motions across the tropopause, that could influence the vertical shear, and in turn turbulence generation in this region. In the next subsection, we explore the shear occurrence in the vicinity of GWs activity.

4.2 GWs related to wind shear

340   We start here with an analysis of vertical wind shear, a key prerequisite for dynamical instability and thus turbulence related to observed GWs.
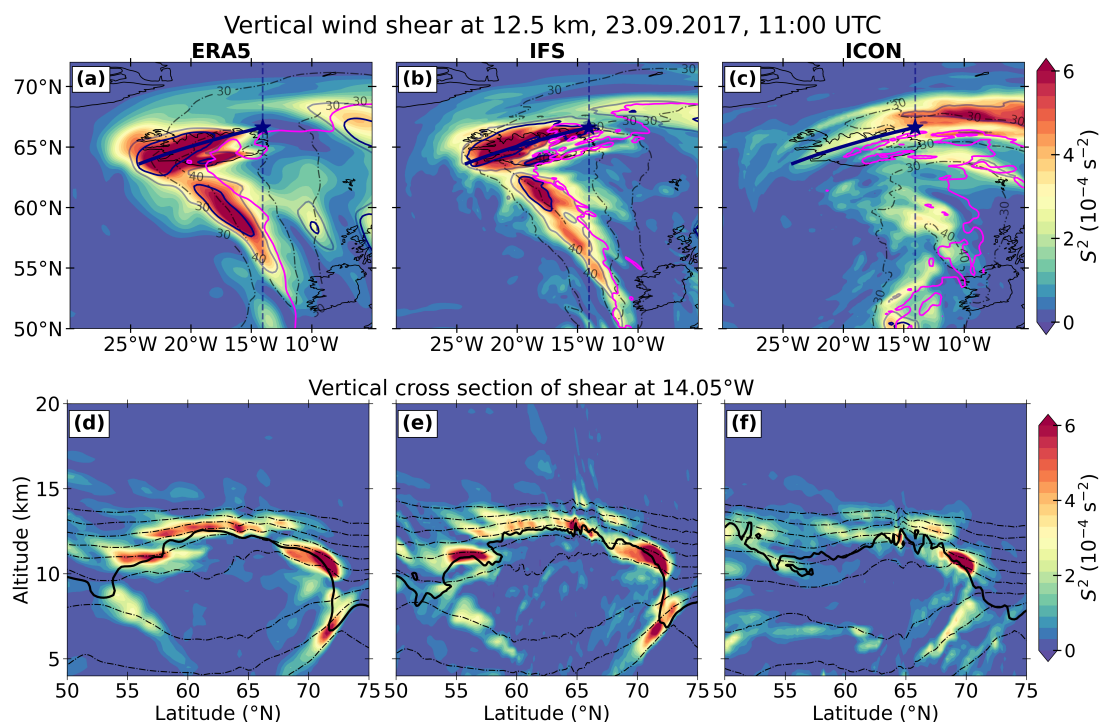

Figure 7. Distribution of vertical wind shear at 12.5 km altitude for (a) ERA5, (b) IFS and (c) ICON. The dashed black lines in upper panel presents the horizontal wind speed for values greater than 30 m s^{-1}, 3.5 PVU isoline in magenta and solid lines represent the Ri<1 (black) and Ri=1.25 (grey) at 12.5 km altitude. The star marker indicates the position of flight at 11 UTC. The corresponding vertical cross sections of vertical shear at 14.05° W is shown in lower panel (d-f). The solid line in lower panel represents the 3.5 PVU as a dynamical tropopause whereas dashed lines represents the potential temperature starting from 280 K (bottom) to 380 K (top) with 10 K increments.

The horizontal (upper panel) and vertical (lower panel) distribution of vertical shear is shown in Fig. 7. In Fig. 7a-c, we see significant shear north of 60° N and particularly in ICON, in the vicinity of GW activity identified in the previous section, i.e., around 65° N and 15° W. As discussed in the paragraph above, IFS shows much more signs of GW activity across the

345   tropopause region and in the lower stratosphere, being an interesting region to further study the GWs role to shear enhancement. Moreover, the jet location in Fig. 7a-c and 3.5 PVU dynamical tropopause in Fig. 7d-f holds important piece of information about the jet disturbances being one of the source region of high shear abundance in this region, particularly around the tropopause fold at around 70° N. Reduced Ri values (in black) are observed in the vicinity of the jet across all datasets, particularly pronounced in ERA5 and IFS, and suggest a widespread potential for the occurrence of dynamic instability (Fig.

350   7a-c). Notable differences are that Ri show low values almost in all regions of enhanced shear for ERA5 and IFS, while these

regions appear more as patches in ICON. In ICON, the regions of low Ri has also advected away from the flight path.

Furthermore, the vertical distribution of shear in ERA5 (Fig. 7d) shows the maximum shear abundance in the ridge and along

the tropopause fold with maximum values reaching up to $6 \times 10^{-4} \mathrm{s}^{-2}$. The maxima in the ridge (around $64°$ N) is in the prox-

imity of GWs which in turn could affect the shear values there. Although the IFS exhibits a pattern of S^2 that closely resembles

355   that of ERA5, the spatial scale of the maxima is notably smaller in the vicinity of the ridge. In ICON, shear maximizes also

in the ridge or tropopause fold area and also shows a second maxima at the elevated tropopause which could be caused by jet

disturbances. Particularly, in the UTLS, the jet-stream on larger scales and GW on smaller scales contribute significantly to the

generation of shear. In principle, all three datasets show countable co-location of shear with GW patterns (Fig. 7d-f) and thus

the shear location related to the phase of GWs modes remain consistent among all datasets. Overall, the upward propagating

360   GW signals observed in Sect. 4.1, indicate a spatiotemporal co-occurrence of GWs and vertical wind shear.

However, this requires further investigation to understand whether the small–scale, vertically propagating GWs observed in

ERA5 are of relevance to the shear generation across the tropopause. One possible explanation for this is that vertically prop-

agating, large amplitude, high vertical (less horizontal) wavelength GWs locally modulate the N^2 in the LMS (Kunkel et al.,

2014; Kaluza et al., 2019; Zhang et al., 2019), which in turn also allows to accumulate vertical shear in this region. This sug-

365   gests that GWs may contribute (or influenced) partially to the vertical shear generation in the lower stratosphere. On the other

hand, the maximum shear in locations other than GW activity, likely generated from the large–scale components including the

jet stream. This further motivates a deeper look at the significance of small–scale GWs to high wind shear, and subsequently

to the potential turbulence occurrence.

4.3   Turbulence diagnostics in the LMS

370   In continuation to turbulence analysis, this section addresses the occurrence of dynamic instability associated with GWs,

particularly in the LMS, as well as the relation between the occurrences of GWs and shear perturbations in terms of 2D

histograms. Also note that the occurrences are retrieved over flight covered region ($50°$N–$72°$N, $5°$W–$30°$W, i.e., blue box in

Fig. 1).

If smaller scales play a major role, we expect a positive correlation between absolute small–scale momentum flux and shear

375   perturbations in terms of turbulence occurrence in the LMS. Qualitatively, we already notice a positive correlation between

shear abundances and GWs in the LMS in all three models. This result supports previous analysis based on idealized studies in

terms of GWs related to the shear and subsequent turbulence (Umbarkar and Kunkel, 2025). Here, we expect ERA5 reanalysis

to resolve the vertical shear in the UTLS similar to the operational IFS data (Kaluza et al., 2019, 2021).

As discussed previously in Sect. 4.1, ERA5 represents the resolved fine scale structures of the GWs, and as such shows the

380   positive correlation between AMF and shear fluctuations (Fig. 8). However, high resolution IFS likely shows more pronounced

$S^{2'}$ and AMF likely due to finer resolution as well as at least well represented GWs in the UTLS than ERA5. In contrast, ICON

exhibits similar relation but with slightly less $S^{2'}$ occurrences and maxima reaching up to $6 \times 10^{-4} s^{-2}$. ICON shows also a

larger AMF compared to the others, which might be related to general differences between IFS and ICON. In ICON, we note
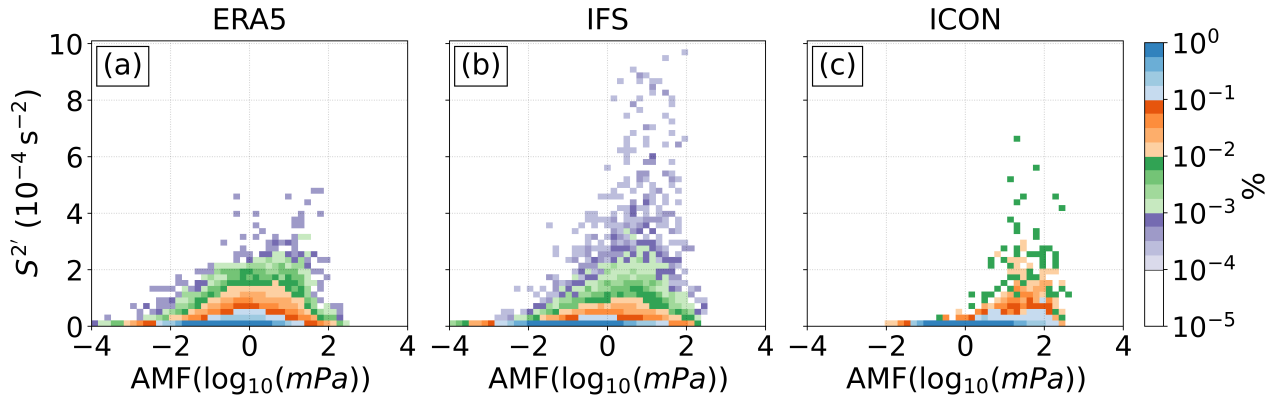
Figure 8. Relative occurrence frequency distribution of absolute momentum flux due to GWs-vertical shear perturbations pair in the LMS for $0 \leq Ri \leq 1$ for different datasets. Normalized counts of PDFs distribution is shown. Logarithmic occurrence frequency color scale is applied.

that shear is more patchy and shows lower values in general (see also Fig. 7c). It will be interesting to see in a follow-up analysis
385 whether this is limited to our case study or represents a more general difference between these modeling systems. Note here
that the ERA5 and IFS shows quite similar relation when looked at the occurrences at the range of 10^{-3} to 10^{-2} (see the green
colors), while the difference in ICON likely arise mainly from the occurrence of low Ri values (see Sect. 4.2). Nonetheless,
ERA5 shows fewer occurrences of maximum shear than IFS. This could be due to its coarser horizontal resolution, which
might lead to the limited representation of (partially resolved) GW spectrum in the UTLS. Overall, these results pinpoints the
390 crucial role of GW-induced shear to the potential turbulence occurrence, and subsequently representing the important role of
GWs to transporting the momentum across the tropopause.

We now turn the attention to the small–scale behavior of GWs, as the GW-induced shear can coincide with the regions of
considerable dynamic instability and potentially influence turbulent mixing. The following section examines CAT and its
spatial relation to GWs.

4.4 Are these GWs responsible for CAT occurrence?

395

One previously suggested impact from inertial instability is that any associated inertia GWs could lead to CAT when these
waves breaks (Knox, 1997). Previously, Thompson and Schultz (2021) showed the emission of inertia GWs, following the
release of inertial instability, instigate light–moderate occurrences of CAT around the unstable region using idealized model
simulations. We widen our analysis by examining both the broader upstream flow patterns and the small–scale disturbances,
400 primarily GWs, that contribute to the development of dynamical instability and potentially to the CAT occurrences in the lower
stratosphere.

Turbulence does not develop as a single continuous area, but in sporadic pockets of light to moderate intensity that persists
for few minutes around the periphery of unstable region (Sharman et al., 2006). Our results from small–scale contribution
show a similar pattern (see Fig. 9). While ERA5 data have an hourly resolution and may limit the representation of such short
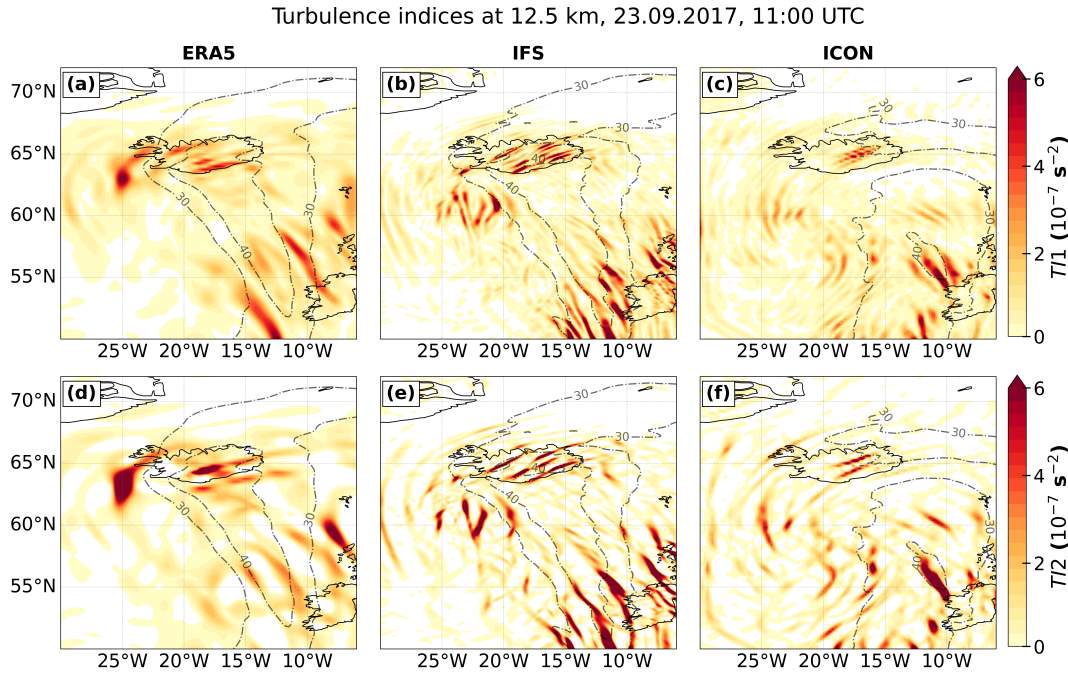
Figure 9. Distribution of turbulent indices TI1 (upper panel) and TI2 (lower panel) at 12.5 km altitude for ERA5 (a, d), IFS (b, e) and ICON (c, f). The dashed black lines presents the horizontal wind speed >30 ms^{-1}.

lived events, the observed structures suggest the conditions conducive to their occurrence, albeit with reduced intensity. As the GWs propagate upward through the tropopause, the wave perturbations significantly modify the local Ri, with the apparent Ri<1 bands are the regions of possible Kelvin-Helmholtz instability (Fig. 7). Subsequently, along the phase lines of GWs, there are apparent bands of enhanced TI1 as well as TI2, which are more prominent in IFS followed by ICON (Fig. 9a-f). Further, higher resolution ICON simulations with nesting revealed that localized volumes of enhanced resolved and subgrid, small–scale turbulence formed in the bands of the reduced Ri (Fig. S7) as well as high TI1 and TI2 (Fig. S8). The enhanced turbulence, especially the CAT was due to the small–scale GWs and it is proposed that such mechanism contributed to the turbulence encountered during the flight.

Calculating the TI1 index as a proxy for CAT from zonal and meridional wind perturbations (u', v'), we find several regions where CAT develops simultaneously across the tropopause. Given that the current study focus on the occurrence frequency of CAT in the UTLS likely near the upper level jet stream, we choose the 95th percentile value of the total occurrences as the thresholds of each CAT index for light-moderate intensity level followed by Lee et al. (2019, 2022). Figure 10 illustrates the frequency distribution of CAT indices over the LMS. We use all data points in the LMS i.e., between 3.5 PVU and 380 K, to derive PDF distribution of the small–scale TI1 and TI2 indices. We then calculate the 95th percentile values of these distributions, which are used as threshold values. The resulting TI1 threshold values for ERA5, IFS and ICON are $1.4 \times 10^{-7}s^{-1}$, $2.1 \times 10^{-7}s^{-1}$ and $1.5 \times 10^{-7}s^{-1}$ respectively. Given the range of values in PDFs and the differences in the underlying
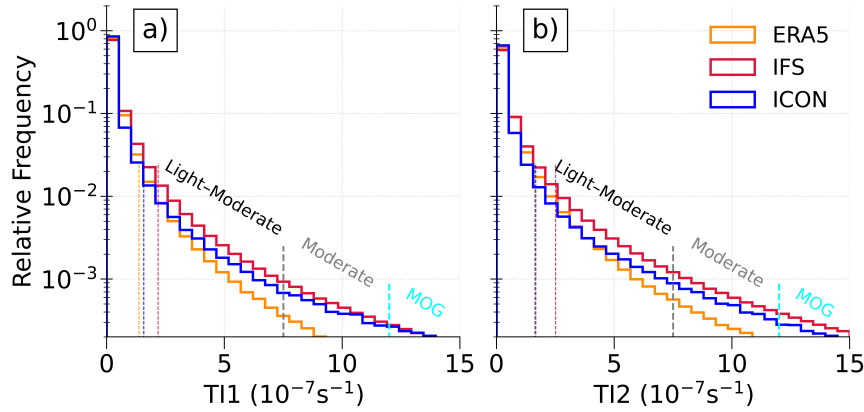
Figure 10. Relative occurrence frequency distribution of (a) TI1 and (b) TI2 for ERA5, IFS and ICON in the LMS domain. Corresponding to histogram, colored dashed lines indicate threshold retrieved as the 95th percentile over the LMS domain that is considered as threshold for light moderate category. Grey and aqua lines represent the threshold for moderate (7.5-12) and moderate to greater MOG (>12) intensity clear air turbulence, respectively.

data, the gained thresholds differ only slightly across the datasets, with some differing up to a factor of two. Furthermore, the more GW related index TI2, gained from the inclusion of convergent flow, applies the same threshold criterion as TI1, where the resulting thresholds are $1.5 \times 10^{-7} s^{-1}$, $2.45 \times 10^{-7} s^{-1}$, and $1.5 \times 10^{-7} s^{-1}$ for ERA5, IFS and ICON, respectively. We categorize the CAT levels based on the thresholds: light to moderate from respective 95th percentile threshold, moderate

425 $(7.5 \times 10^{-7} s^{-1}$ to $12 \times 10^{-7} s^{-1})$, and moderate-or-greater (MOG) ($>12 \times 10^{-7} s^{-1}$), consistent with previous studies (e.g., Ellrod and Knapp, 1992; Thompson and Schultz, 2021).

Collating all turbulence occurrence throughout the simulation, as seen in Fig. 10a, we find that most occurrences fall into this light–moderate category, but some occurrences of moderate intensity are also found which are more pronounced in the IFS, but less apparent in ERA5. Nonetheless, the moderate to greater (MOG) intensity CAT in TI1 with slightly less occurrences are

430 strong in the positive tail of the TI2 (Fig. 10b). Interestingly, there is also increase in the TI2 occurrences observed with ERA5. Furthermore, the more pronounced moderate-level CAT with GWs formulation, i.e., TI2 (see Fig. 10b), suggests a probable contribution of GWs to CAT development. One possible explanation for this could be that GWs over Iceland observed in the IFS lead to the maximum shear perturbations as well as pronounced TI1 and TI2, which further induce strong potential instability and ultimately result in the development of higher risk CAT.

435 Figure 11 show the 2D probability distribution of TI1-AMF and TI2-AMF pairs in the LMS domain. Moreover, as discussed above, if the subgrid or small scales plays a major role, the positive relation between AMF and turbulent indices is expected. When we investigate this relation in the LMS, we observed the positive correlation between occurrence frequencies of these two quantities. There are smaller values for TI1/TI2 in ERA5. Whereas, the IFS and ICON shows similarity in terms of occurrences of maxima of TI1, slight variations are observed in the higher occurrences of TI2 among these datasets. That is to say, the ICON

440 and IFS shows similarity in terms of abundance of TI1 and AMF above the threshold, indicating light to moderate level CAT.
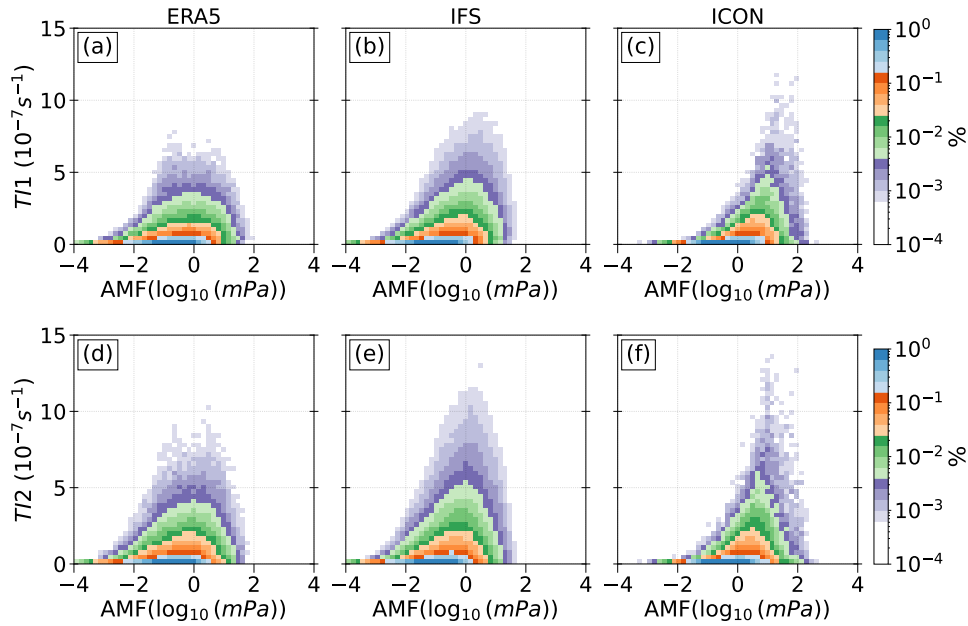
19

Figure 11. Frequency (%) distribution of absolute momentum flux-Turbulent indices TI1 (a-c), TI2 (d-f) in pairs over the LMS for (a, d) ERA5, (b, e) IFS and (c, f) ICON datasets. Normalized counts of PDFs distribution is shown. Logarithmic occurrence frequency color scale is applied.

When looking at the TI2, while ERA5 shows slightly less occurrence in this case, its maxima reaches moderate intensity CAT in both IFS and ICON (Fig. 11d-f). However, this picture contrasts with Fig. 8 in Sect. 4.3, where ICON exhibits weaker and patchier shear perturbations compared to ERA5 and IFS in the vicinity of low Ri. One plausible explanation is that local flow deformation in ICON exhibit enhanced values during turbulent events in the LMS, partly compensating for weaker resolved shear, thereby causing higher abundance of TI1 in the vicinity of GWs. Nonetheless, the forecast skill of DEF as a turbulence diagnostic has previously been linked to frontogenesis, enhancement of thermal wind shear (Ellrod and Knapp, 1992), and local GW activity (Kunkel et al., 2014).

Overall, following the positive relation between small–scale shear and AMF in the LMS above the North Atlantic as discussed in Sect. 4.3, we can go even one step further. The relationship observed between the turbulence indices, TI1 and TI2, and GWs, leads us to conclude that GW play a role for the occurrence of CAT in our analysis region, as evidenced by the positive correlation between turbulence diagnostics and the AMF.

4.5 Turbulence diagnostics in a zonal framework

Finally, we turn our perspective to the more general feature which has been described recently in Kaluza et al. (2021, 2022). We first examine the occurrence of extratropical TSL (Kaluza et al., 2021) across three available datasets. Afterwards, we investigate the role of GWs in the formation of the TSL and whether turbulence occurs in the region of the TSL.
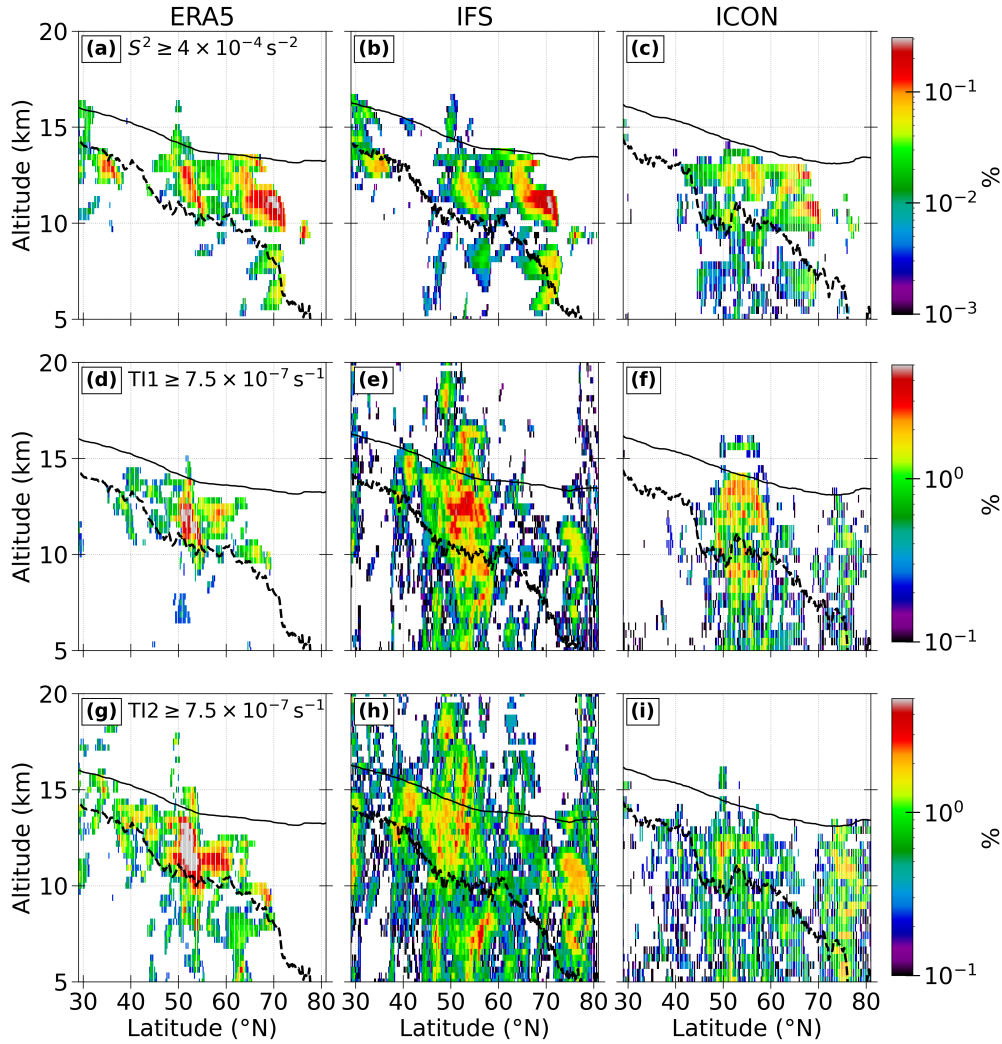
Figure 12. Relative occurrence frequency distribution of grid volumes that exhibit (a-c) $S^2 \geq 4 \times 10^{-4} s^{-2}$, (d-f) TI1 $\geq 7.5 \times 10^{-7} s^{-1}$ and (g-i) TI2 $\geq 7.5 \times 10^{-7} s^{-1}$ over the North Atlantic domain on 23rd September 2017, 11:00 UTC for ERA5, IFS, and ICON. Panels (d–i) represent regions of moderate-intensity CAT occurrence. The occurrence frequencies are shown with logarithmic frequency contours, displaying the data in bins of sizes $\Delta y = 0.2°$ and $\Delta z = 500\,m$. The zonal-mean dynamical tropopause (3.5 PVU isosurface; black dashed line) and the zonal-mean 380 K isentrope of potential temperature (solid line) are overlaid.

We first start with the shear abundance in the extratropics. The TSL has been defined via an exceeding of a defined threshold value of vertical wind shear, i.e., $S^2 \geq S_t^2$ where $S_t^2 = 4 \times 10^{-4} s^{-2}$ (Kaluza et al., 2021). We apply an analogous method to our case study at an instantaneous time step in our limited area over the North Atlantic at which we observed the GW-induced shear enhancement.

460

21

Figure 12a-c shows the relative occurrence frequencies counted in zonal direction for S^2 exceeding the threshold, i.e., $S^2 \geq S_t^2$. The datasets represents both upper tropospheric as well as lower stratospheric occurrence frequency distribution of strong shear. The above average dynamical tropopause altitude for profiles with $S^2 \geq S_t^2$ are indicative of the modulation of the tropopause by baroclinic wave ridges and the associated GW activity (see Sect. 4.1 and 4.2). Moreover, the pronounced shear occurrences

465 are observed in between 45° N and 60° N in ERA5 and IFS, and with slightly less abundance in ICON. This further supports the results observed in Sect. 4.3, where the LMS exhibit the high abundance of shear as well as GW momentum flux in the vicinity of potential turbulence.

We further explore this relation through the zonal occurrence of CAT indices, that means for TI1 exceeding the threshold, TI1 $\geq 7.5 \times 10^{-7} s^{-1}$, correspond to moderate category CAT occurrences (Fig.12d-f). In the zonally integrated view of TI1, we

470 observed the substantial TI1 occurrences at and farther northward to the highly sheared regions. Note here that both TI1 and TI2 exhibit identical pattern in terms of occurrences in the LMS (compare Fig. 12d-f and g-i). In ERA5, enhanced frequencies indicate an abundance of moderate level CAT out of total potential CAT occurrences, see the region around 50° N in the LMS. IFS rather shows the pronounced CAT between 45° N and 60° N (Fig. 12e), with wider spread out in TI2 occurrences (Fig. 12h). In contrast to the similarities noted between ICON and IFS in Sect. 4.4, here ICON exhibits slightly lower occurrences

475 of CAT indices which are weaker but broadly distributed in TI2 (Fig. 12f, i). Besides this, regions with enhanced shear but absent TI1 occurrences (e.g., near 35° N and 70° N in ERA5 and IFS) point to shear generated by large–scale features such as the jet stream, rather than by GWs. In sum, the turbulence diagnostics reveal turbulence hotspots near typical aircraft cruising altitudes ($\sim$ 10-13.5 km) in the North Atlantic across all datasets, consistent with the altitude range where strong shear layers frequently occur.

480 Question remains whether the GWs are of any relevance to the extratropical TSL and now to the CAT hotspots. The shorter GWs that propagate more vertically carry a greater absolute momentum flux. If GWs plays a role, we could expect at least quasi-spatial co-occurrence of above observed enhanced shear and high intensity turbulent indices with GW momentum flux. Figure 13 represents AMF in the shear-dominated regions as well in the moderate intensity CAT prone region. The AMF in the vicinity of strong shear highlights predominantly enhanced flux above the tropopause in ERA5 and IFS, particularly in the

485 midlatitude belt (Fig. 13a, b). It is worth noting that, ERA5 exhibits a pattern akin to IFS, albeit with less spatial resolution. Meanwhile ICON exhibits more localized but more intense AMF in the vicinity of strong shear (Fig. 13c). The observed fluxes suggest strong GWs activity associated with baroclinic disturbances. Interestingly, the areas of pronounced shear are mostly also the regions of highly amplified GW activity. This overlap confirms the aforementioned relationship between GWs and enhanced shear and gives the plausibility of the significant contribution of small–scales to turbulent mixing. This findings

490 further agree with the conclusion of the previous studies of baroclinic life cycles (Kaluza et al., 2019, 2021) and process study (Kunkel et al., 2019; Umbarkar and Kunkel, 2025).

Finally, the relation between GWs and CAT is assessed by the AMF in the vicinity of TI1 (Fig. 13d-f) and TI2 (Fig. 13g-i). In ERA5, turbulence hotspots coincide with strong GW activity, with GW fluxes dominating across the tropopause and at the LMS. Next, IFS exhibits broader AMF spectrum characterized by strong vertical gradient in the vicinity of higher TI1 and

495 a wider spatial extent in TI2 (Fig. 13e, h). In contrast, ICON exhibits more intense small–scale flux structures and vertical
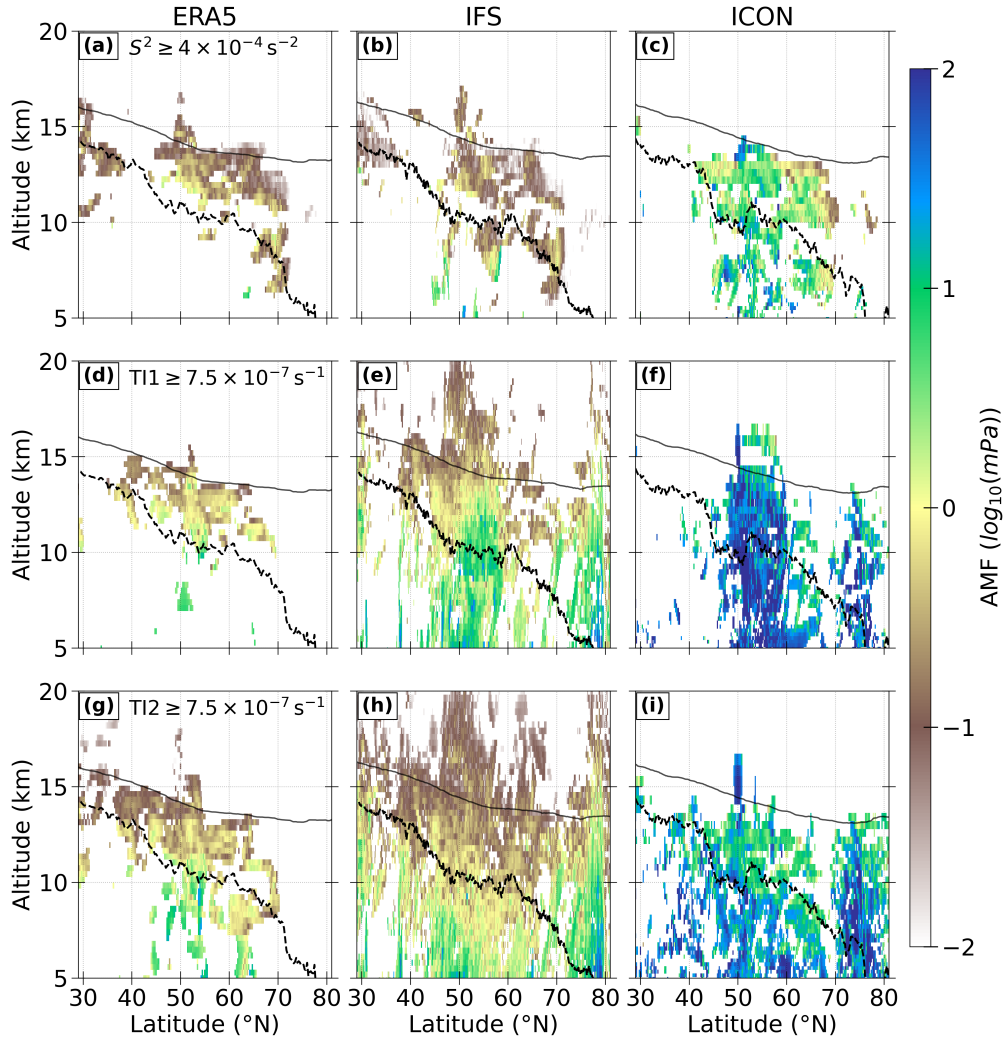
Figure 13. Zonal mean resolved GW absolute momentum flux (AMF, $log_{10}(mPa)$) values conditioned on regions where (a-c) $S^2 \geq S_t^2$, (d-f) TI1 $\geq 7.5 \times 10^{-7} s^{-1}$ and (g-i) TI2 $\geq 7.5 \times 10^{-7} s^{-1}$. All values are vertically binned with dz=500 m. The zonal-mean dynamical tropopause (3.5 PVU isosurface; black dashed line) and the zonal-mean 380 K isentrope of potential temperature (solid line) are overlaid.

gradients throughout the UTLS, could be associated with resolved GWs (Fig. 13f, i). In principle, there are observed higher vertical gradients of AMF where we have enhanced (clear–air) turbulence. This distinction underlines the specific contribution of GWs to the observed turbulence hotspots.

Besides this, some uncertainty remains in the quantitative assessment of GW momentum fluxes, as the representation of unre-
500 solved sources may affect both their magnitude and distribution. An important note is that ICON has been shown to reproduce satellite-derived GW flux patterns without requiring additional parameterizations for unresolved waves over the middle strato-sphere (Stephan et al., 2019b). However, Toghraei et al. (2025) suggests that its non-orographic parameterizations may under-

estimate the dynamical filtering of westward-propagating waves in the mid-latitude region. Nonetheless, the enhanced wave momentum fluxes co-located with regions of high TI1 occurrence, supports the link between GW activity and CAT generation
505 in the UTLS.

Overall, these findings support the hypothesis that subgrid or small–scale GWs contribute substantially to the enhanced shear formation, the development of high intensity CAT, and hence, consequently could contribute to shaping the ExTL dynamics.

5   Discussion and conclusion

The present study highlights the role of gravity wave induced shear as a key parameter for the tropopause shear layer (TSL,
510 Kaluza et al., 2021) on the basis of observations, reanalysis and forecast data. We note that this is key for the potential occurrence of clear air turbulence, as highly transient yet frequent mixing processes in the extratropical lowermost stratosphere. As such these processes may play a crucial role in the formation and maintenance of extratropical tropopause transition layer, alongside other processes such as convective injection.

Based on idealized studies of the GW–scale cascade process in Umbarkar and Kunkel (2025), we here examine this relation
515 in depth in a more realistic environment, for the atmospheric state over the North Atlantic during an episode of the airborne mission WISE. On the one side we use airborne measurements and additionally the output of three gridded model data sets, i.e., ERA5 reanalysis, ECMWF IFS forecast and an ICON forecast dataset. Specifically, we use time series analysis, trace species profiles, tracer tracer correlations and spectral analysis as well as a recently explored hybrid approach based on Helmholtz decomposition method (Wei et al., 2022), to answer our questions. In summary, we come to the following results:

520   ○ Observations show mixed air masses in the vicinity of vertical shear and GW occurrence. We analyzed a flight of the WISE campaign over the North Atlantic, where tracer-tracer correlations of CO and N_2O revealed the occurrence of mixed air masses. Vertical profiles of these trace gases indicated that these mixed air masses resided in the LMS between 345 K and 375 K. Further analysis revealed that the mixing might be in relation to GWs and that the mixing occurred very recently in regions of persistently low Richardson numbers and enhanced vertical wind shear.

525   ○ Despite their different resolutions the dynamical situation is represented very similar in ERA5, IFS and ICON. However, the differences in ERA5 and IFS appear mainly in the representation of mesoscale features which is mainly attributable to the varying underlying resolution. Larger differences between ICON and the ECMWF models appear in the representation of vertical shear and Richardson numbers, which is however not the case anymore for the turbulence indices TI1 and TI2.

530   ○ ERA5, despite its coarser horizontal resolution, captures upward propagating large–amplitude GWs, which further affect the vertical gradients of the wind components that lead to shear generation. However, it shows slightly less vertical shear occurrences than high-resolution IFS data, likely due to insufficient or partial (resolved) representation of GWs in the UTLS. ICON exhibits slightly lower shear occurrences, raising a question of whether resolving smaller-scale GWs redistributes variance and reduces diagnosed shear. Taken together, these behaviors indicate partially resolved GW

535   spectra across datasets. Nonetheless, compared with its predecessors, ERA5 captures a larger portion of GW spectrum providing valuable information on the spectral characteristics of GWs and is therefore suitable for long term analysis of GW-induced shear, at least over the North Atlantic.

○ The high-resolution IFS and ICON datasets reproduced a large-amplitude GW event on 23rd September 2017 over the North Atlantic reasonably well. Application of vertical momentum fluxes and shear perturbations analysis, tracer-tracer
540   correlations, flow instability as well as turbulent metrics point to multiscale interactions dominated by small–scale GWs.

○ Turbulence prone GW–induced enhanced shear highly correlates with appearance of envelopes (or packets) of small–scale GWs of ~100 km of wavelength in the LMS with the same characteristics. Spectral function detects downscale energy transfer from small–scale GWs that intensifies shear near ~340 K, thereby creating conditions conducive to the generation of (clear-air) turbulence.

545   ○ The diagnosed turbulent regions display strongly banded structures associated with GWs and GW-induced shear, parallel to the upper-level front, that is closely linked to baroclinic activity and associated tropopause variability (Kaluza et al., 2021). ERA5 and IFS indicate widespread potential for the occurrence of dynamic instability, while ICON shows weaker shear perturbations but higher AMF at low Ri. Regarding CAT indices, ERA5 shows signatures of moderate intensity CAT in the LMS associated with strong GW activity, with IFS and ICON mimic this pattern but with slightly intense
550   high-risk CAT. In sum, this highlights the substantial role of GWs in enhancing shear and fostering high-intensity CAT in the LMS, with ERA5 capturing both GW spectra and their contribution to shear and turbulence, making it suitable for long-term studies over the North Atlantic.

The relation between small–scale GW momentum flux has long been used as a reliable index for GW analysis (Plougonven et al., 2003, 2017; Lachnitt et al., 2023; Umbarkar and Kunkel, 2025), hinting towards the possibility for the active role of GWs
555   in producing shear hotspots and thereby to the subsequent mixing in the lowermost stratosphere. However, further research should address the seasonal and geographical variability of small–scale, GW–induced shear over the mid-latitude region.
The similarities and differences we find here are certainly model, resolution and parameterization dependent. While ICON demonstrates skill in reproducing observed GW flux patterns, questions remain as to whether resolved GW amplitudes in the extratropics are fully converged across resolutions, and how parameterized sources interact with the resolved spectrum. To a
560   certain extent, this is supported by the fact that high-resolution simulations have not yet converged when it comes to GWs in the extratropics (Polichtchouk et al., 2023; Gupta et al., 2024).
In summary, the resulting picture presented by a synthesis of our findings in one cascade of processes across scales: starting with inertia GWs associated with the flow imbalance, proceeding through the generation of enhanced shear mechanism, with excitation of shear instabilities at the small scales where potential turbulence was generated and ending with the energy-
565   momentum transfer in the vertical. In conclusion, our analysis highlights GW-induced shear as a driver of UTLS transport and mixing, as well as a source of high-risk CAT occurrences, meriting further investigation into its prevalence in the geographic location and its potential implications for both climate processes, particularly the redistribution of H_2O and O_3 and their

associated radiative forcing, and aviation forecasting. Overall, the GW related processes should be considered as the important candidate for the interpretation of CAT in the extratropical UTLS.

Appendix A: Supporting information to the selected methodology to retrieve the large–scale background flow and the short-scale perturbations

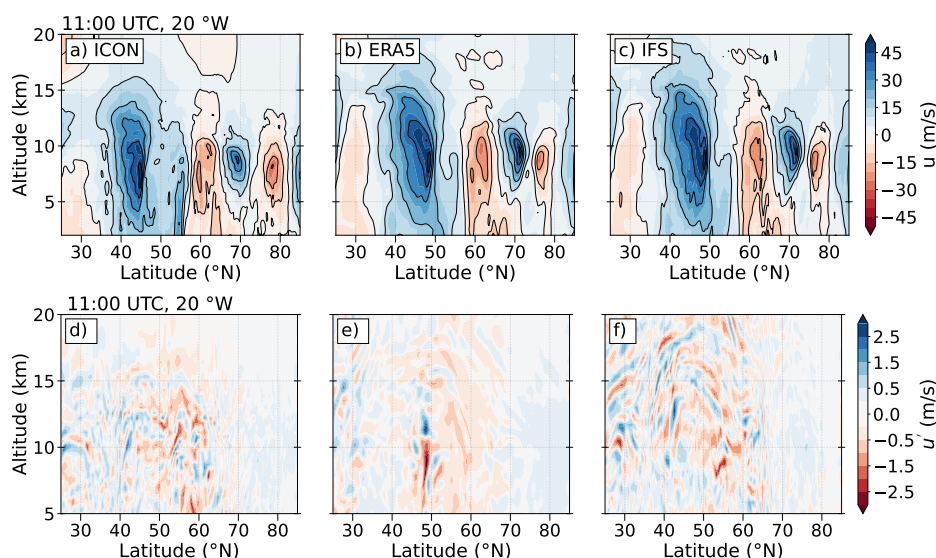**Figure A1.** Vertical cross section of zonal wind u (upper panel) and retrieved u perturbations (lower panel) on 23 September 2017 11:00 UTC at 20°W for (a, d) ICON, (b, e) ERA5, and (c, f) IFS.

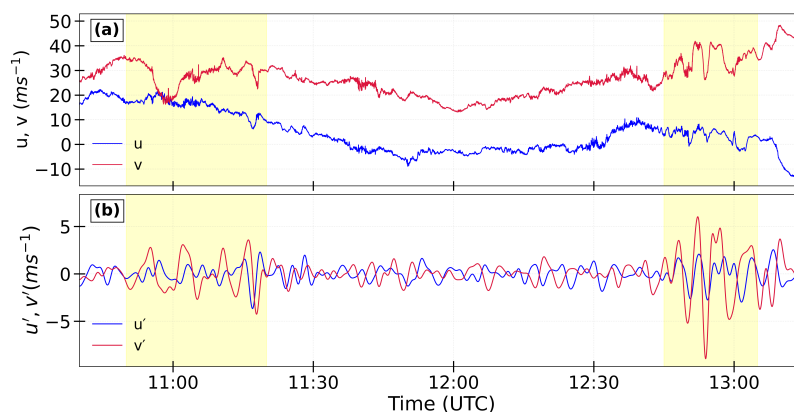# Appendix B: Supporting information to the hodograph analysis

Figure B1. Time series of (a) zonal (u, ms^{-1}; blue) and meridional (v, ms^{-1}; red) wind component from HALO for WISE RF05, the shaded yellow regions same as Fig. 3, whereas panel (b) shows perturbation of u and v obtained from Butterworth filter.

Author contributions. MU and DK conceptualized the core research questions and goals. CS and AM set up and conducted the ICON
580 simulations. TK, HCL, and PH provided the WISE campaign data. MU performed the data analysis, post-processing, and prepared the initial
draft of the manuscript. MU and DK jointly revised and edited the manuscript. All authors contributed to and commented on the manuscript.

Competing interests. The authors have no conflict of interest.

References

590 Achatz, U., Alexander, M. J., Becker, E., Chun, H. Y., Dörnbrack, A., Holt, L., Plougonven, R., Polichtchouk, I., Sato, K., Sheshadri, A., Stephan, C. C., Van Niekerk, A., and Wright, C. J.: Atmospheric Gravity Waves: Processes and Parameterization, Journal of the Atmospheric Sciences, 81, 237–262, https://doi.org/10.1175/JAS-D-23-0210.1, 2024.

Alexander, M. J. and Grimsdell, A. W.: Seasonal cycle of orographic gravity wave occurrence above small islands in the Southern Hemisphere: Implications for effects on the general circulation, Journal of Geophysical Research: Atmospheres, 118,
595 https://doi.org/10.1002/2013jd020526, 2013.

Alexander, M. J., Geller, M., McLandress, C., Polavarapu, S., Preusse, P., Sassi, F., Sato, K., Eckermann, S., Ern, M., Hertzog, A., Kawatani, Y., Pulido, M., Shaw, T. A., Sigmond, M., Vincent, R., and Watanabe, S.: Recent developments in gravity-wave effects in climatemodels and the global distribution of gravity-wavemomentum flux from observations and models, Quarterly Journal of the Royal Meteorological Society, 136, 1103–1124, https://doi.org/10.1002/qj.637, 2010.

600 Appenzeller, C., Holton, J. R., and Rosenlof, K. H.: Seasonal variation of mass transport across the tropopause, Journal of Geophysical Research: Atmospheres, 101, 15 071–15 078, https://doi.org/10.1029/96jd00821, 1996.

Berthet, G., Esler, J. G., and Haynes, P. H.: A Lagrangian perspective of the tropopause and the ventilation of the lowermost stratosphere, Journal of Geophysical Research: Atmospheres, 112, https://doi.org/10.1029/2006jd008295, 2007.

Birner, T.: Fine-scale structure of the extratropical tropopause region, Journal of Geophysical Research Atmospheres, 111, 1–14,
605 https://doi.org/10.1029/2005JD006301, 2006.

Birner, T., Dörnbrack, A., and Schumann, U.: How sharp is the tropopause at midlatitudes?, Geophysical Research Letters, 29, 1–4, https://doi.org/10.1029/2002GL015142, 2002.

Dörnbrack, A.: Transient Tropopause Waves, Journal of the Atmospheric Sciences, 81, 1647–1668, https://doi.org/10.1175/jas-d-24-0037.1, 2024.

610 Dörnbrack, A., Bechtold, P., and Schumann, U.: High-Resolution Aircraft Observations of Turbulence and Waves in the Free Atmosphere and Comparison With Global Model Predictions, Journal of Geophysical Research: Atmospheres, 127, https://doi.org/10.1029/2022jd036654, 2022.

Dörnbrack, A., Lachnitt, H., Hoor, P., and Imazio, P. R.: Multiscale Dynamical Processes Shaping a Mixing Line, Journal of Geophysical Research: Atmospheres, 130, https://doi.org/10.1029/2025jd043527, 2025.

615 Durran, D. R.: Pseudomomentum Diagnostics for Two-Dimensional Stratified Compressible Flow, Journal of Atmospheric Sciences, 52, 3997 – 4009, https://doi.org/10.1175/1520-0469(1995)052<3997:PDFTDS>2.0.CO;2, 1995.

Ellrod, G. P. and Knapp, D. I.: An Objective Clear-Air Turbulence Forecasting Technique: Verification and Operational Use, Weather and Forecasting, 7, 150–165, https://doi.org/10.1175/1520-0434(1992)007<0150:aocatf>2.0.co;2, 1992.

Fritts, D. C. and Alexander, M. J.: Gravity wave dynamics and effects in the middle atmosphere, Reviews of Geophysics, 41, 1–64,
620 https://doi.org/10.1029/2001RG000106, 2003.

Geller, M. A., Alexander, M. J., Love, P. T., Bacmeister, J., Ern, M., Hertzog, A., Manzini, E., Preusse, P., Sato, K., Scaife, A. A., and Zhou, T.: A Comparison between Gravity Wave Momentum Fluxes in Observations and Climate Models, Journal of Climate, 26, 6383–6405, https://doi.org/10.1175/jcli-d-12-00545.1, 2013.

Gomes, M. B., Shapiro, A., Parsons, D. B., and Gebauer, J. G.: Using a Numerical Model to Evaluate a Proposed Mechanism for Nocturnal
625   Low-Level Jets and Ascent over a Warm Tongue, Monthly Weather Review, 153, 1265–1281, https://doi.org/10.1175/mwr-d-24-0111.1,
2025.

Guest, F. M., Reeder, M. J., Marks, C. J., and Karoly, D. J.: Inertia–Gravity Waves Observed in the Lower Stratosphere over Macquarie
Island, Journal of the Atmospheric Sciences, 57, 737–752, https://doi.org/10.1175/1520-0469(2000)057<0737:igwoit>2.0.co;2, 2000.

Gultepe, I., Sharman, R., Williams, P. D., Zhou, B., Ellrod, G., Minnis, P., Trier, S., Griffin, S., Yum, S. S., Gharabaghi, B., Feltz, W.,
630   Temimi, M., Pu, Z., Storer, L. N., Kneringer, P., Weston, M. J., Chuang, H.-y., Thobois, L., Dimri, A. P., Dietz, S. J., França, G. B.,
Almeida, M. V., and Neto, F. L. A.: A Review of High Impact Weather for Aviation Meteorology, Pure and Applied Geophysics, 176,
1869–1921, https://doi.org/10.1007/s00024-019-02168-6, 2019.

Gupta, A., Birner, T., Dörnbrack, A., and Polichtchouk, I.: Importance of Gravity Wave Forcing for Springtime Southern Polar Vortex
Breakdown as Revealed by ERA5, Geophysical Research Letters, 48, https://doi.org/10.1029/2021GL092762, 2021.

635 Gupta, A., Sheshadri, A., Alexander, M. J., and Birner, T.: Insights on Lateral Gravity Wave Propagation in the Extratropical Stratosphere
From 44 Years of ERA5 Data, Geophysical Research Letters, 51, https://doi.org/10.1029/2024gl108541, 2024.

Hegglin, M. I., Boone, C. D., Manney, G. L., and Walker, K. A.: A global view of the extratropical tropopause transition layer from Atmo-
spheric Chemistry Experiment Fourier Transform Spectrometer O3, H2O, and CO, Journal of Geophysical Research Atmospheres, 114,
1–18, https://doi.org/10.1029/2008JD009984, 2009.

640 Heller, R., Voigt, C., Beaton, S., Dörnbrack, A., Giez, A., Kaufmann, S., Mallaun, C., Schlager, H., Wagner, J., Young, K., and Rapp,
M.: Mountain waves modulate the water vapor distribution in the UTLS, Atmospheric Chemistry and Physics, 17, 14 853–14 869,
https://doi.org/10.5194/acp-17-14853-2017, 2017.

Hersbach, H., Bell, B., Berrisford, P., Hirahara, S., Horányi, A., Muñoz-Sabater, J., Nicolas, J., Peubey, C., Radu, R., Schepers, D., Simmons,
A., Soci, C., Abdalla, S., Abellan, X., Balsamo, G., Bechtold, P., Biavati, G., Bidlot, J., Bonavita, M., De Chiara, G., Dahlgren, P., Dee,
645   D., Diamantakis, M., Dragani, R., Flemming, J., Forbes, R., Fuentes, M., Geer, A., Haimberger, L., Healy, S., Hogan, R. J., Hólm, E.,
Janisková, M., Keeley, S., Laloyaux, P., Lopez, P., Lupu, C., Radnoti, G., de Rosnay, P., Rozum, I., Vamborg, F., Villaume, S., and Thépaut,
J.: The ERA5 global reanalysis, Quarterly Journal of the Royal Meteorological Society, 146, 1999–2049, https://doi.org/10.1002/qj.3803,
2020.

Hirota, I. and Niki, T.: Inertia-Gravity Waves in the Troposphere and Stratosphere Observed by the MU Radar, Journal of the Meteorological
650   Society of Japan. Ser. II, 64, 995–999, https://doi.org/10.2151/jmsj1965.64.6_995, 1986.

Holton, J. R., Haynes, P. H., McIntyre, M. E., Douglass, A. R., Rood, R. B., and Pfister, L.: Stratosphere-troposphere exchange, Reviews of
Geophysics, 33, 403–439, https://doi.org/10.1029/95RG02097, 1995.

Hooke, W. H.: Gravity Waves, p. 272–288, American Meteorological Society, ISBN 9781935704201, https://doi.org/10.1007/978-1-935704-
20-1_12, 1986.

655 Hoor, P., Gurk, C., Brunner, D., Hegglin, M. I., Wernli, H., and Fischer, H.: Seasonality and extent of extratropical TST derived from in-situ
CO measurements during SPURT, Atmospheric Chemistry and Physics, 4, 1427–1442, https://doi.org/10.5194/acp-4-1427-2004, 2004.

Hoor, P., Wernli, H., Hegglin, M. I., and Bönisch, H.: Transport timescales and tracer properties in the extratropical UTLS, Atmospheric
Chemistry and Physics, 10, 7929–7944, https://doi.org/10.5194/acp-10-7929-2010, 2010.

Jewtoukoff, V., Hertzog, A., Plougonven, R., Cámara, A. d. l., and Lott, F.: Comparison of Gravity Waves in the Southern Hemisphere Derived
660   from Balloon Observations and the ECMWF Analyses, Journal of the Atmospheric Sciences, 72, 3449–3468, https://doi.org/10.1175/jas-
d-14-0324.1, 2015.

Jovanovic, G.: Gravity waves as a mechanism of troposphere–stratosphere–mesosphere coupling during sudden stratospheric warming, Atmospheric Chemistry and Physics, 25, 2979–2988, https://doi.org/10.5194/acp-25-2979-2025, 2025.

Kaluza, T., Kunkel, D., and Hoor, P.: Composite analysis of the tropopause inversion layer in extratropical baroclinic waves, Atmospheric
665   Chemistry and Physics, 19, 6621–6636, https://doi.org/10.5194/acp-19-6621-2019, 2019.

Kaluza, T., Kunkel, D., and Hoor, P.: On the occurrence of strong vertical wind shear in the tropopause region: a 10-year ERA5 northern hemispheric study, Weather and Climate Dynamics, 2, 631–651, https://doi.org/10.5194/wcd-2-631-2021, 2021.

Kaluza, T., Kunkel, D., and Hoor, P.: Analysis of Turbulence Reports and ERA5 Turbulence Diagnostics in a Tropopause-Based Vertical Framework, Geophysical Research Letters, 49, https://doi.org/10.1029/2022gl100036, 2022.

670   Kim, J.-H., Sharman, R., Strahan, M., Scheck, J. W., Bartholomew, C., Cheung, J. C. H., Buchanan, P., and Gait, N.: Improvements in Nonconvective Aviation Turbulence Prediction for the World Area Forecast System, Bulletin of the American Meteorological Society, 99, 2295–2311, https://doi.org/10.1175/bams-d-17-0117.1, 2018.

Kim, Y., Eckermann, S. D., and Chun, H.: An overview of the past, present and future of gravity-wave drag parametrization for numerical climate and weather prediction models, Atmosphere-Ocean, 41, 65–98, https://doi.org/10.3137/ao.410105, 2003.

675   Knox, J. A.: Possible Mechanisms of Clear-Air Turbulence in Strongly Anticyclonic Flows, Monthly Weather Review, 125, 1251–1259, https://doi.org/10.1175/1520-0493(1997)125<1251:pmocat>2.0.co;2, 1997.

Koch, S. E., Jamison, B. D., Lu, C., Smith, T. L., Tollerud, E. I., Girz, C., Wang, N., Lane, T. P., Shapiro, M. A., Parrish, D. D., and Cooper, O. R.: Turbulence and Gravity Waves within an Upper-Level Front, Journal of the Atmospheric Sciences, 62, 3885–3908, https://doi.org/10.1175/jas3574.1, 2005.

680   Krautstrunk, M. and Giez, A.: The Transition From FALCON to HALO Era Airborne Atmospheric Research, p. 609–624, Springer Berlin Heidelberg, ISBN 9783642301834, https://doi.org/10.1007/978-3-642-30183-4_37, 2012.

Kruse, C. G. and Smith, R. B.: Gravity Wave Diagnostics and Characteristics in Mesoscale Fields, Journal of the Atmospheric Sciences, 72, 4372–4392, https://doi.org/10.1175/jas-d-15-0079.1, 2015.

Kunkel, D., Hoor, P., and Wirth, V.: Can inertia-gravity waves persistently alter the tropopause inversion layer?, Geophysical Research
685   Letters, 41, 7822–7829, https://doi.org/10.1002/2014GL061970, 2014.

Kunkel, D., Hoor, P., and Wirth, V.: The tropopause inversion layer in baroclinic life-cycle experiments: The role of diabatic processes, Atmospheric Chemistry and Physics, 16, 541–560, https://doi.org/10.5194/acp-16-541-2016, 2016.

Kunkel, D., Hoor, P., Kaluza, T., Ungermann, J., Kluschat, B., Giez, A., Lachnitt, H. C., Kaufmann, M., and Riese, M.: Evidence of small-scale quasi-isentropic mixing in ridges of extratropical baroclinic waves, Atmospheric Chemistry and Physics, 19, 12 607–12 630,
690   https://doi.org/10.5194/acp-19-12607-2019, 2019.

Lachnitt, H. C.: Consistent meteorological (ERA5) and chemical (CLaMS) information across airborne measurements over the globe between 1997 and 2023, Zenodo [data set], https://doi.org/10.5281/ZENODO.15076520, (last access: 08 September 2025), 2025.

Lachnitt, H. C., Hoor, P., Kunkel, D., Bramberger, M., Dörnbrack, A., Müller, S., Reutter, P., Giez, A., Kaluza, T., and Rapp, M.: Gravity-wave-induced cross-isentropic mixing: A DEEPWAVE case study, Atmospheric Chemistry and Physics, 23, 355–373,
695   https://doi.org/10.5194/acp-23-355-2023, 2023.

Lane, T. P. and Sharman, R. D.: Gravity wave breaking, secondary wave generation, and mixing above deep convection in a three-dimensional cloud model, Geophysical Research Letters, 33, https://doi.org/10.1029/2006gl027988, 2006.

Lane, T. P., Reeder, M. J., and Clark, T. L.: Numerical Modeling of Gravity Wave Generation by Deep Tropical Convection, Journal of the Atmospheric Sciences, 58, 1249–1274, https://doi.org/10.1175/1520-0469(2001)058<1249:nmogwg>2.0.co;2, 2001.

700 Lane, T. P., Doyle, J. D., Plougonven, R., Shapiro, M. A., and Sharman, R. D.: Observations and Numerical Simulations of Iner-
     tia–Gravity Waves and Shearing Instabilities in the Vicinity of a Jet Stream, Journal of the Atmospheric Sciences, 61, 2692–2706,
     https://doi.org/10.1175/jas3305.1, 2004.

     Lee, D.-B., Chun, H.-Y., and Kim, J.-H.: Evaluation of Multimodel-Based Ensemble Forecasts for Clear-Air Turbulence, Weather and Fore-
     casting, 35, 507–521, https://doi.org/10.1175/waf-d-19-0155.1, 2019.

705 Lee, J. H., Kim, J., Sharman, R. D., Kim, J., and Son, S.: Climatology of Clear-Air Turbulence in Upper Troposphere and Lower
     Stratosphere in the Northern Hemisphere Using ERA5 Reanalysis Data, Journal of Geophysical Research: Atmospheres, 128,
     https://doi.org/10.1029/2022jd037679, 2022.

     Lehmann, C. I., Kim, Y.-H., Preusse, P., Chun, H.-Y., Ern, M., and Kim, S.-Y.: Consistency between Fourier transform and small-volume
     few-wave decomposition for spectral and spatial variability of gravity waves above a typhoon, Atmospheric Measurement Techniques, 5,
710 1637–1651, https://doi.org/10.5194/amt-5-1637-2012, 2012.

     Müller, S., Hoor, P., Berkes, F., Bozem, H., Klingebiel, M., Reutter, P., Smit, H. G. J., Wendisch, M., Spichtinger, P., and Borrmann, S.: In
     situ detection of stratosphere-troposphere exchange of cirrus particles in the midlatitudes, Geophysical Research Letters, 42, 949–955,
     https://doi.org/10.1002/2014gl062556, 2015.

     Olsen, M. A., Douglass, A. R., and Kaplan, T. B.: Variability of extratropical ozone stratosphere–troposphere exchange using microwave limb
715 sounder observations, Journal of Geophysical Research: Atmospheres, 118, 1090–1099, https://doi.org/10.1029/2012jd018465, 2013.

     O'sullivan, D. and Dunkerton, T. J.: Generation of Inertia–Gravity Waves in a Simulated Life Cycle of Baroclinic Instability, Journal of
     Atmospheric Sciences, 52, 3695 – 3716, https://doi.org/10.1175/1520-0469(1995)052<3695:GOIWIA>2.0.CO;2, 1995.

     Pan, L. L., Randel, W. J., Gary, B. L., Mahoney, M. J., and Hintsa, E. J.: Definitions and sharpness of the extratropical tropopause: A trace
     gas perspective, Journal of Geophysical Research: Atmospheres, 109, https://doi.org/10.1029/2004jd004982, 2004.

720 Pan, L. L., Konopka, P., and Browell, E. V.: Observations and model simulations of mixing near the extratropical tropopause, Journal of
     Geophysical Research Atmospheres, 111, 1–15, https://doi.org/10.1029/2005JD006480, 2006.

     Plougonven, R. and Snyder, C.: Gravity waves excited by jets: Propagation versus generation, Geophysical Research Letters, 32,
     https://doi.org/10.1029/2005gl023730, 2005.

     Plougonven, R. and Zhang, F.: Internal gravity waves from atmospheric jets and fronts, Reviews of Geophysics, 52, 33–76,
725 https://doi.org/10.1002/2012rg000419, 2014.

     Plougonven, R., Teitelbaum, H., and Zeitlin, V.: Inertia gravity wave generation by the tropospheric midlatitude jet as given
     by the Fronts and Atlantic Storm-Track Experiment radio soundings, Journal of Geophysical Research: Atmospheres, 108,
     https://doi.org/10.1029/2003jd003535, 2003.

     Plougonven, R., Hertzog, A., and Teitelbaum, H.: Observations and simulations of a large-amplitude mountain wave breaking over the
730 Antarctic Peninsula, Journal of Geophysical Research Atmospheres, 113, 1–17, https://doi.org/10.1029/2007JD009739, 2008.

     Plougonven, R., Jewtoukoff, V., Cámara, A. d. l., Lott, F., and Hertzog, A.: On the Relation between Gravity Waves and Wind Speed in
     the Lower Stratosphere over the Southern Ocean, Journal of the Atmospheric Sciences, 74, 1075–1093, https://doi.org/10.1175/jas-d-16-
     0096.1, 2017.

     Polichtchouk, I., van Niekerk, A., and Wedi, N.: Resolved Gravity Waves in the Extratropical Stratosphere: Effect of Horizontal Resolution
735 Increase from O(10) to O(1) km, Journal of the Atmospheric Sciences, 80, 473–486, https://doi.org/10.1175/jas-d-22-0138.1, 2023.

     Rapp, M., Kaifler, B., Dörnbrack, A., Gisinger, S., Mixa, T., Reichert, R., Kaifler, N., Knobloch, S., Eckert, R., Wildmann, N., Giez, A.,
     Krasauskas, L., Preusse, P., Geldenhuys, M., Riese, M., Woiwode, W., Friedl-Vallon, F., Sinnhuber, B.-M., Torre, A. d. l., Alexander, P.,

Hormaechea, J. L., Janches, D., Garhammer, M., Chau, J. L., Conte, J. F., Hoor, P., and Engel, A.: SOUTHTRAC-GW: An Airborne Field Campaign to Explore Gravity Wave Dynamics at the World's Strongest Hotspot, Bulletin of the American Meteorological Society, 102, E871–E893, https://doi.org/10.1175/bams-d-20-0034.1, 2021.

740

Riese, M., Ploeger, F., Rap, A., Vogel, B., Konopka, P., Dameris, M., and Forster, P.: Impact of uncertainties in atmospheric mixing on simulated UTLS composition and related radiative effects, Journal of Geophysical Research: Atmospheres, 117, https://doi.org/10.1029/2012jd017751, 2012.

Schwenk, C. and Miltenberger, A.: The role of ascent timescales for warm conveyor belt (WCB) moisture transport into the upper troposphere

745

and lower stratosphere (UTLS), Atmospheric Chemistry and Physics, 24, 14073–14099, https://doi.org/10.5194/acp-24-14073-2024, 2024.

Schwenk, C. and Miltenberger, A.: The role of ascent timescales for warm conveyor belt (WCB) moisture transport into the upper troposphere and lower stratosphere (UTLS), Zenodo [data set], https://doi.org/10.5281/ZENODO.14924689, (last access: 08 September 2025), 2025.

Shapiro, M. A.: Further Evidence of the Mesoscale and Turbulent Structure of Upper Level Jet Stream–Frontal Zone Systems, Monthly

750

Weather Review, 106, 1100–1111, https://doi.org/10.1175/1520-0493(1978)106<1100:feotma>2.0.co;2, 1978.

Shapiro, M. A.: Turbulent Mixing within Tropopause Folds as a Mechanism for the Exchange of Chemical Constituents between the Stratosphere and Troposphere, Journal of the Atmospheric Sciences, 37, 994–1004, https://doi.org/10.1175/1520-0469(1980)037<0994:tmwtfa>2.0.co;2, 1980.

Sharman, R., Tebaldi, C., Wiener, G., and Wolff, J.: An Integrated Approach to Mid- and Upper-Level Turbulence Forecasting, Weather and

755

Forecasting, 21, 268–287, https://doi.org/10.1175/waf924.1, 2006.

Sharman, R. D. and Pearson, J. M.: Prediction of Energy Dissipation Rates for Aviation Turbulence. Part I: Forecasting Nonconvective Turbulence, Journal of Applied Meteorology and Climatology, 56, 317–337, https://doi.org/10.1175/jamc-d-16-0205.1, 2017.

Sharman, R. D., Cornman, L. B., Meymaris, G., Pearson, J., and Farrar, T.: Description and Derived Climatologies of Automated In Situ Eddy-Dissipation-Rate Reports of Atmospheric Turbulence, Journal of Applied Meteorology and Climatology, 53, 1416–1432,

760

https://doi.org/10.1175/jamc-d-13-0329.1, 2014.

Spreitzer, E., Attinger, R., Boettcher, M., Forbes, R., Wernli, H., and Joos, H.: Modification of potential vorticity near the tropopause by nonconservative processes in the ECMWF model, Journal of the Atmospheric Sciences, 76, 1709–1726, https://doi.org/10.1175/JAS-D-18-0295.1, 2019.

Stephan, C. C., Strube, C., Klocke, D., Ern, M., Hoffmann, L., Preusse, P., and Schmidt, H.: Intercomparison of Gravity Waves in Global

765

Convection-Permitting Models, Journal of the Atmospheric Sciences, 76, 2739–2759, https://doi.org/10.1175/jas-d-19-0040.1, 2019a.

Stephan, C. C., Strube, C., Klocke, D., Ern, M., Hoffmann, L., Preusse, P., and Schmidt, H.: Gravity Waves in Global High-Resolution Simulations With Explicit and Parameterized Convection, Journal of Geophysical Research: Atmospheres, 124, 4446–4459, https://doi.org/10.1029/2018jd030073, 2019b.

Strube, C., Ern, M., Preusse, P., and Riese, M.: Removing spurious inertial instability signals from gravity wave temperature perturbations

770

using spectral filtering methods, Atmospheric Measurement Techniques, 13, 4927–4945, https://doi.org/10.5194/amt-13-4927-2020, 2020.

Thompson, C. F. and Schultz, D. M.: The Release of Inertial Instability Near an Idealized Zonal Jet, Geophysical Research Letters, 48, https://doi.org/10.1029/2021gl092649, 2021.

Toghraei, I., Lott, F., Köhler, L., Stephan, C. C., and Alexander, M. J.: Can Parameterizations Reproduce the Gravity Wave Momentum Fluxes and Drag Simulated by a Global High-Resolution Model?, Geophysical Research Letters, 52, https://doi.org/10.1029/2025gl115499, 2025.

775 Trier, S. B., Sharman, R. D., MuñOz-Esparza, D., and Lane, T. P.: Environment and mechanisms of severe turbulence in a midlatitude
cyclone, Journal of the Atmospheric Sciences, 77, 3869–3889, https://doi.org/10.1175/JAS-D-20-0095.1, 2020.

Umbarkar, M.: Data used for paper "Evidence of gravity wave contribution to vertical shear and mixing in the lower stratosphere: a WISE
case study", Zenodo [data set], https://doi.org/10.5281/ZENODO.17227439, 2025.

Umbarkar, M. and Kunkel, D.: Contribution of gravity waves to shear in the extratropical lowermost stratosphere: insights from idealized
780 baroclinic life cycle experiments, Atmospheric Chemistry and Physics, 25, 10 159–10 182, https://doi.org/10.5194/acp-25-10159-2025,
2025.

Wang, M. and Fu, Q.: Stratosphere-Troposphere Exchange of Air Masses and Ozone Concentrations Based on Reanalyses and Observations,
Journal of Geophysical Research: Atmospheres, 126, https://doi.org/10.1029/2021jd035159, 2021.

Wang, S. and Zhang, F.: Sensitivity of Mesoscale Gravity Waves to the Baroclinicity of Jet-Front Systems, Monthly Weather Review, 135,
785 670–688, https://doi.org/10.1175/mwr3314.1, 2007.

Wei, J., Zhang, F., and Richter, J. H.: An Analysis of Gravity Wave Spectral Characteristics in Moist Baroclinic Jet–Front Systems, Journal
of the Atmospheric Sciences, 73, 3133–3155, https://doi.org/10.1175/jas-d-15-0316.1, 2016.

Wei, J., Zhang, F., Richter, J. H., Alexander, M. J., and Sun, Y. Q.: Global Distributions of Tropospheric and Stratospheric Grav-
ity Wave Momentum Fluxes Resolved by the 9-km ECMWF Experiments, Journal of the Atmospheric Sciences, 79, 2621–2644,
790 https://doi.org/10.1175/jas-d-21-0173.1, 2022.

Weyland, F., Hoor, P., Kunkel, D., Birner, T., Plöger, F., and Turhal, K.: Long-term changes in the thermodynamic structure of the lowermost
stratosphere inferred from reanalysis data, Atmospheric Chemistry and Physics, 25, 1227–1252, https://doi.org/10.5194/acp-25-1227-
2025, 2025.

Whiteway, J. A., Pavelin, E. G., Busen, R., Hacker, J., and Vosper, S.: Airborne measurements of gravity wave breaking at the tropopause,
795 Geophysical Research Letters, 30, 2–6, https://doi.org/10.1029/2003GL018207, 2003.

Whiteway, J. A., Klaassen, G. P., Bradshaw, N. G., and Hacker, J.: Transition to turbulence in shear above the tropopause, Geophysical
Research Letters, 31, 2–5, https://doi.org/10.1029/2003GL018509, 2004.

Yoshida, L., Tomikawa, Y., Ejiri, M. K., Tsutsumi, M., Kohma, M., and Sato, K.: Large-Amplitude Inertia Gravity Waves Over
Syowa Station: Comparison of PANSY Radar and ERA5 Reanalysis Data, Journal of Geophysical Research: Atmospheres, 129,
800 https://doi.org/10.1029/2023jd040490, 2024.

Zängl, G., Reinert, D., Rípodas, P., and Baldauf, M.: The <scp>ICON</scp> (ICOsahedral Non-hydrostatic) modelling framework of
<scp>DWD</scp> and <scp>MPI-M</scp>: Description of the non-hydrostatic dynamical core, Quarterly Journal of the Royal Mete-
orological Society, 141, 563–579, https://doi.org/10.1002/qj.2378, 2014.

Zhang, F., Davis, C. A., Kaplan, M. L., and Koch, S. E.: Wavelet analysis and the governing dynamics of a large-amplitude mesoscale
805 gravity-wave event along the East Coast of the United States, Quarterly Journal of the Royal Meteorological Society, 127, 2209–2245,
https://doi.org/10.1002/qj.49712757702, 2001.

Zhang, F., Wei, J., Zhang, M., Bowman, K. P., Pan, L. L., Atlas, E., and Wofsy, S. C.: Aircraft measurements of gravity waves in the
upper troposphere and lower stratosphere during the START08 field experiment, Atmospheric Chemistry and Physics, 15, 7667–7684,
https://doi.org/10.5194/acp-15-7667-2015, 2015a.

810 Zhang, W., Peng, J., Zhang, W., Wang, S., Li, Z., and Hanyan, W.: Sensitivity of Gravity Wave Momentum Flux Estimates on Separation
Methods, Monthly Weather Review, 153, 1721–1742, https://doi.org/10.1175/mwr-d-24-0272.1, 2025.

Zhang, Y., Zhang, S., Huang, C., Huang, K., Gong, Y., and Gan, Q.: The interaction between the tropopause inversion layer and the inertial gravity wave activities revealed by radiosonde observations at a midlatitude station, Journal of Geophysical Research: Atmospheres, 120, 8099–8111, https://doi.org/10.1002/2015jd023115, 2015b.

815 Zhang, Y., Zhang, S., Huang, C., Huang, K., and Gong, Y.: The Tropopause Inversion Layer Interaction With the Inertial Gravity Wave Activities and Its Latitudinal Variability, Journal of Geophysical Research: Atmospheres, 124, 7512–7522, https://doi.org/10.1029/2019JD030309, 2019.

Zülicke, C. and Peters, D.: Simulation of inertia-gravity waves in a poleward-breaking Rossby wave, Journal of the Atmospheric Sciences, 63, 3253–3276, https://doi.org/10.1175/JAS3805.1, 2006.